Development of Water-Soluble Ln^{3+}-doped LaF_3 Nanoparticles as Potential Biolabels.

by

Peter Robert Diamente
B.Sc., Carleton University, 2001

A Thesis Submitted in Partial Fulfillment of the
Requirements for the Degree of

MASTER OF SCIENCES

in the Department of Chemistry

Supervisor: Dr. ir. Frank C.J.M. van Veggel (Department of Chemistry)

ABSTRACT

The use of optically robust, luminescent lanthanide-based particles is becoming an area of interest for biolabel-related chemistry, due to their long lifetimes and range of non-overlapping absorption and emission lines from the visible to the near-infrared. Reported here, is the synthesis and optical properties of water-soluble, luminescent Ln^{3+}-doped nanoparticles (NPs) coordinated with a hydrophilic $(RO)PO_3^{2-}$ ligand, that facilitates the stabilization of the NPs in aqueous conditions, and that regulates particle growth to the nanometer range. The use of lanthanide ions as dopants, in particular Eu^{3+} and Er^{3+} ions, yields optically robust particles with narrow emission lines in the visible (591 nm) and in the near-infrared (1530 nm), respectively. Luminescent lifetimes range from the microsecond to the millisecond range for Er^{3+} and Eu^{3+} ions, respectively. Surface functionalization of the NPs was carried out by using biotin-based derivatives for biotin-avidin binding studies.

Supervisor: Dr. ir. Frank C.J.M. van Veggel (Department of Chemistry)

Acknowledgements

First and foremost, I would like to thank my supervisor Dr. ir. Frank C.J.M. van Veggel for his guidance, patience, and wisdom that allowed me to stay focused during my studies. Also, I would like to thank Dr. R.D. Burke for his helpful suggestions for the different possible directions that could be used for surface-functionalization of the nanoparticles. Additionally, I would like to thank Dr. C. Bohne for her suggestions with regards to troubleshooting both our fluorescence data and the fluorometer itself. I am especially grateful for all the help that Siva, Sudarsan, Venkat, and Wiljan have given me over the past two years. Finally, thanks to the chemistry staff for their help in various areas that have helped me to complete this thesis.

Table of Contents

List of Figures

List of Tables

Chapter 1

Luminescence of Lanthanide Ions

1.1 General introduction to lanthanide properties

Many luminescent lanthanide ions have desirable properties, such as luminescence ranging from the visible to the near-infrared, long-lived luminescent lifetimes, and resilience to photobleaching, yet use of these ions has often been limited due to their low molar absorption coefficients. The energy levels of some of the trivalent lanthanide ions are depicted in Figure 1.1 for Pr^{3+}, Nd^{3+}, Sm^{3+}, Eu^{3+}, Gd^{3+}, Tb^{3+}, Dy^{3+}, Ho^{3+}, Er^{3+}, Tm^{3+} and Yb^{3+}.[1] Each line in the absorption spectrum corresponds to an individual energy level inside the 4f shell, while the luminescence spectrum corresponds to the transitions between two energy levels, but not necessarily involving the ground state. The nomenclature used describe each level is referred to as $^{2S+1}L_J$ levels according to Russell-Saunders coupling schemes, where S is the spin multiplicity, L is the orbital angular momentum, and J is the total angular momentum.

For f-element ions in solids, especially trivalent lanthanide ions, the electronic transitions only have a weak coupling to lattice vibrations and electric fields due to the 4f electrons being shielded by the 5s and 5p electrons.[2] However, despite the weak ion-lattice interaction, this perturbation is responsible for the spectral fine structure in which the optical spectra of f-f transitions have extremely sharp lines almost of atomic characteristics.

When a trivalent lanthanide ion is located at a crystal-lattice site with perfect symmetry, the transitions between the intra-4f levels in the ion are strictly parity-forbidden by LaPorte selection rules, whereby no change in angular momentum (L) between the ground state 4f and the excited state 4f occurs (ie: gerade ↔ gerade or ungerade ↔ ungerade). However, if the ion is in a lattice lacking inversion symmetry, the forbidden transitions are relaxed due to the mixing of opposite parity states into the $4f^n$ configuration, due to an asymmetric crystal field.[3] As a result, the observed transitions for lanthanide ions are a result of magnetic dipole (MD) transitions, induced electric dipole (ED) transitions, and electric quadrupole (EQ) transitions.[4] Of the three, the MD and ED are studied the most due to the luminescent intensity of the transition and the structural information that they provide.

The selection rules typically used for the assignment of the transition levels are as follows: $\Delta S = 0$, $\Delta L = 0$ and $\Delta J = 0, \pm 1$ where the $J = 0 \leftrightarrow J' = 0$ is forbidden for MD transitions. The ED transitions have $\Delta S = 0$, $|\Delta L| \leq 6$, $|\Delta J| \leq 6$, with $|\Delta J| = 2, 4, 6$ if $J = 0$ or $J' = 0$. In both cases, the selection rules are only valid in the Russell-Saunders coupling schemes. Though the selection rules for ΔS and ΔL can be relaxed, the selection rule for J can only be broken down by J-mixing, which is a weak effect due to the crystal field perturbations (vide supra). Consequently, using Eu^{3+} as an example, this J-mixing effect allows the ${}^5D_0$-${}^7F_0$ transition to occur by mixing of the $4f^6$ states into ${}^7F_0$ and ${}^5D_0$ states, resulting in the ${}^5D_0$-${}^7F_0$ transition borrowing intensity from the ${}^5D_0$-${}^7F_J$ transitions ($J = 2, 4, 6$) and from the ${}^5D_J$-${}^7F_0$ transitions ($J = 2, 4$).[4]

Finally, the appearance of the transitions from ${}^5D_0$-${}^7F_0$ and ${}^5D_0$-${}^7F_3$ can not be accounted for by either the MD mechanisms or Judd-Ofelt theory, but is explained by indicating that these transitions "borrow" intensity from the $^5D_0$-$^7F_2$ transition through higher order perturbations by the crystal field.[5,8]

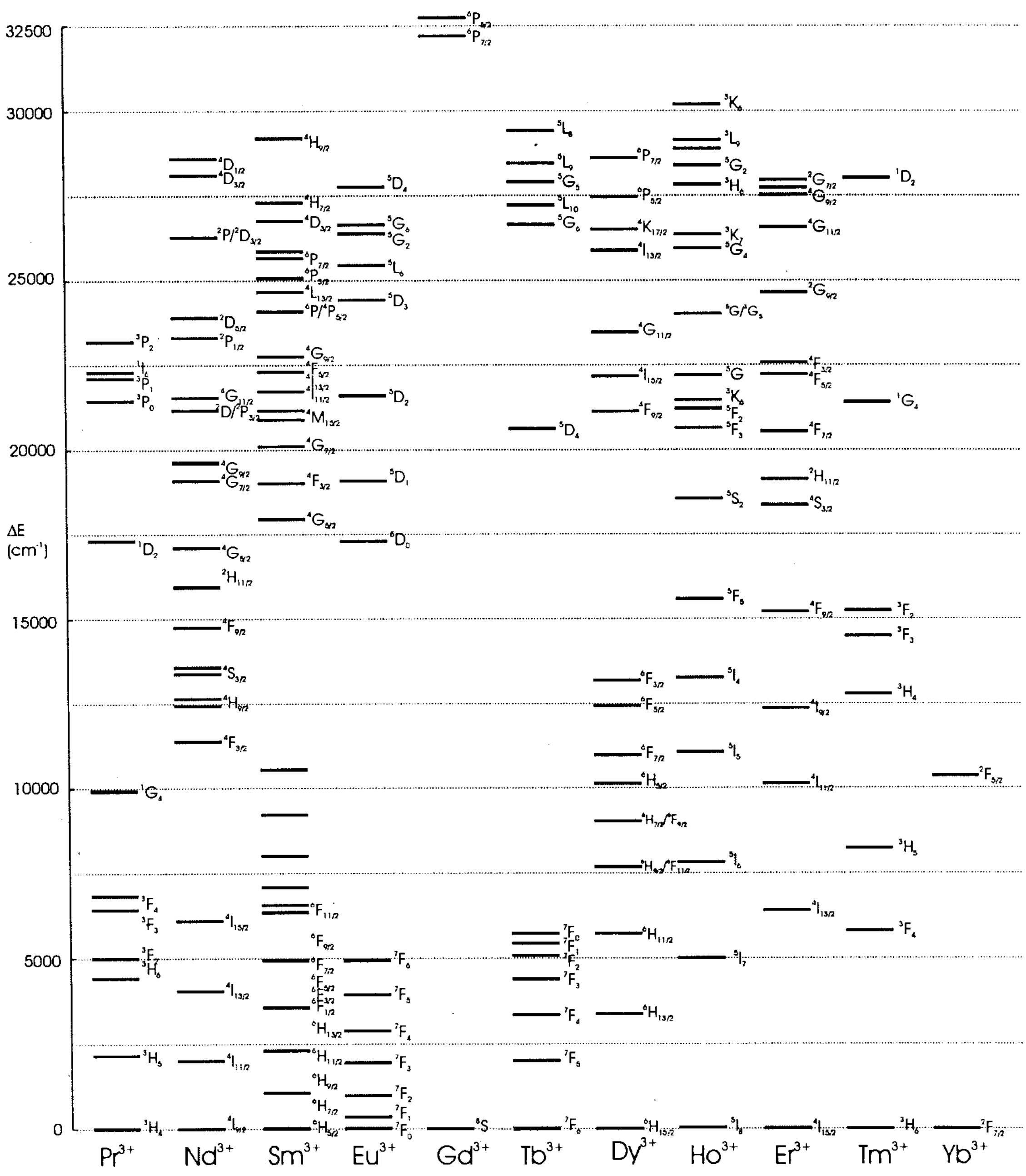

Energy levels in aqueous solution Ref: *J. Chem. Phys.* **1975**, 62, 208.

Figure 1.1: Energy level of selected lanthanide ions.

1.2 Eu^{3+} ion as a probe for structural information

Qualitative information about the nature and symmetry of the Eu^{3+} ion is determined by analyzing both the shape of the non-degenerate $^5D_0$-$^7F_0$ transition at 578 nm, and the $^5D_0$-$^7F_2$/$^5D_0$-$^7F_1$ (I_{7F2}/I_{7F1}) intensity ratio. Most transitions exhibit fine structure, where the ligand field splits up the ^7F_J level into at most 2J+1 sub-levels depending on the symmetry around the ion. However, the non-degenerate $^5D_0$-$^7F_0$ does not exhibit crystal field splitting, and as such, any structure on this band directly indicates the presence of at least two different emitting species.[8]

An example of this behaviour has been studied in nanocrystalline Y_2O_3:Eu systems where a shift in the $^5D_0$-$^7F_0$ transition is a result of Eu^{3+} ions being located in two different areas of the nanocrystals (NC); those towards the surface (yet bound within the NC) and those towards the centre of the NC.[6,7] Furthermore, due to the high surface-to-volume ratio of the NC, as compared to the bulk, surface defects will be more pronounced due to the reduction in emitting ions from the middle of the NC, as compared to the bulk, which otherwise blurs the shifted emission from the surface-bound ions. However, reversal of this argument where the absence of a band indicates there is only one emitting species should be used with caution, due to the observation of some Eu^{3+} complexes that do not (or weakly) show a $^5D_0\rightarrow{}^7F_0$ transition band, as reported by others. 8

Although only a few magnetic dipole transitions exists for the trivalent lanthanide ions, MD transitions are of interest because their intensities are independent of the ligand environment and can thus be used as an intensity standard.[4] However, the induced electric dipole (ED) transition of Eu^{3+} ion is also a *hypersensitive* transition,[8] where the transition is very sensitive to the environment, when coordinated to a ligand, as compared to a free ion in solution (intensity can increase by a factor of 200). As a result, information about the environment of the Eu^{3+} ion (nature and symmetry of the first coordination sphere) can be obtained by analysing the measured intensities of the $^5D_0 \rightarrow {}^7F_2$ and $^5D_0 \rightarrow {}^7F_1$ transitions (I_{7F2}/I_{7F1} intensity ratio).

For Eu^{3+} complexes, several factors affect intensity of the hypersensitive transition: i) symmetry of the coordination sphere, ii) polarizability of the coordinating groups, iii) solvation of the complexes, and iv) the coordination number of Eu^{3+}. Work done by van Veggel et al.[24] reported that polydentate *m*-terphenyl-based Eu^{3+} complexes formed with various ligands, ranging from phenanthroline derivatives, azatriphenylene derivatives and β-diketonate derivatives, yielded I_{7F2}/I_{7F1} intensity ratios that varied from 4.9 to 11.4, as compared to the "bare" (without any of the above three derivatives) with a measured ratio of 3.5.

Ion	**Transition**	***ca.* cm^{-1}**	**Ion**	**Transition**	***ca.* cm^{-1}**
Pr^{3+}	$^3F_2 \leftarrow {}^3H_4$	5,200	Tb^{3+}	None Reported	
Nd^{3+}	$^4G_{5/2} \leftarrow {}^4I_{9/2}$	17,300	Dy^{3+}	$^6F_{11/2} \leftarrow {}^6H_{15/2}$	7,700
Pm^{3+}	$^5G_2, {}^5G_3 \leftarrow {}^5I_4$	18,000	Ho^{3+}	$^5G_6 \leftarrow {}^5I_8$ $^3H_6 \leftarrow {}^5I_8$	22,100 27,700
Sm^{3+}	$^4F_{1/2}, {}^4F_{3/2} \leftarrow {}^6H_{5/2}$	6,400	Er^{3+}	$^2H_{11/2} \leftarrow {}^4I_{15/2}$ $^4G_{11/2} \leftarrow {}^4I_{15/2}$	19,200 26,400
Eu^{3+}	$^5D_1 \leftarrow {}^7F_1$ $^5D_2 \leftarrow {}^7F_0$ $^5D_0 \rightarrow {}^7F_2$	18,700 21,500 16,300	Tm^{3+}	$^3F_4 \leftarrow {}^3H_6$ $^3H_4 \leftarrow {}^3H_6$ $^1G_4 \leftarrow {}^3H_6$	5,900 12,700 21,300
Gd^{3+}	$^6P_{5/2}, {}^6P_{7/2} \leftarrow {}^8S_{7/2}$	32,500			

Table 1.1: List of hypersensitive transitions for trivalent lanthanide ions[4]

Shown in Table 1.1 is a list of other known hypersensitive transitions for trivalent lanthanide ions. In some cases, the transitions show hypersensitivity only in the presence of some particular ligand and the coordination symmetry of the lanthanide ion. Work done by Jorgensen and Judd noted that all known hypersensitive transitions abide by the following selections rules: $|\Delta S| = 0$, $|\Delta L| \leq 2$, and $|\Delta J| \leq 2$.[4]

Although the focus of this thesis is on the development of lanthanide-based nanoparticles (NPs), the following sections will cover some of the historical developments of water-soluble lanthanide-based complexes, in order to give the reader some perspective as to the other directions of research pursued in the field. For a review of the development of various water-soluble lanthanide-based NPs, with emphasis on their use in biological labelling applications, please refer to Chapter 2.

1.3 Antenna ligands for sensitized emission

Use of lanthanide ions in high through-put biological applications, such as immunoassays, is limited because of efficient luminescence quenching by energy loss to high frequency vibrational modes such as OH quenching, and due to the weak absorption of lanthanide ions.[9] In principle, the problems can be overcome by coordinating the lanthanide ion to an antenna ligand, by which sensitized emission can occur. This method uses a ligand (sensitizer) that absorbs the excitation energy efficiently, transfers the energy (usually) from its triplet state to the lanthanide ion, which results in lanthanide ion emission, as depicted in Figure 1.2. This process can occur by either direct coordination of the sensitizing compound to the lanthanide ion, or by the covalent attachment of the sensitizing compounds to an organic ligand, which is able to complex a lanthanide ion.[9,10]

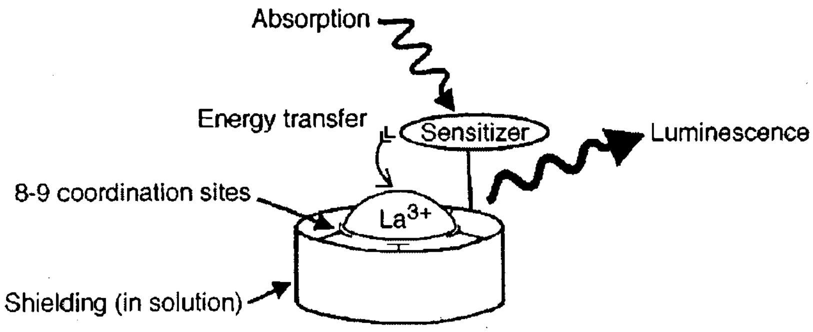

Figure 1.2: Schematic diagram of sensitized emission by the attachment of an antenna ligand to the lanthanide ion, resulting in strong luminescence from the lanthanide ion.[10]

Often these complexes are considered to be light-conversion molecular devices because they are able to transform light absorbed by the ligand into light emitted via intramolecular energy transfer.[11] In light conversion processes, three main factors determine luminescent efficiency: (1) the efficiency of the ligand absorption, (2) the efficiency of the ligand-to-ion energy transfer, and (3) the efficiency of the metal luminescence. A generalized scheme of the photophysical process of sensitized emission is presented in Figure 1.3: the sensitizer (a chromophoric ligand) is excited to its first singlet state, which is often followed by intersystem crossing (ISC) to its triplet state, followed by energy transfer (ET) to the lanthanide ion, and subsequent lanthanide emission.

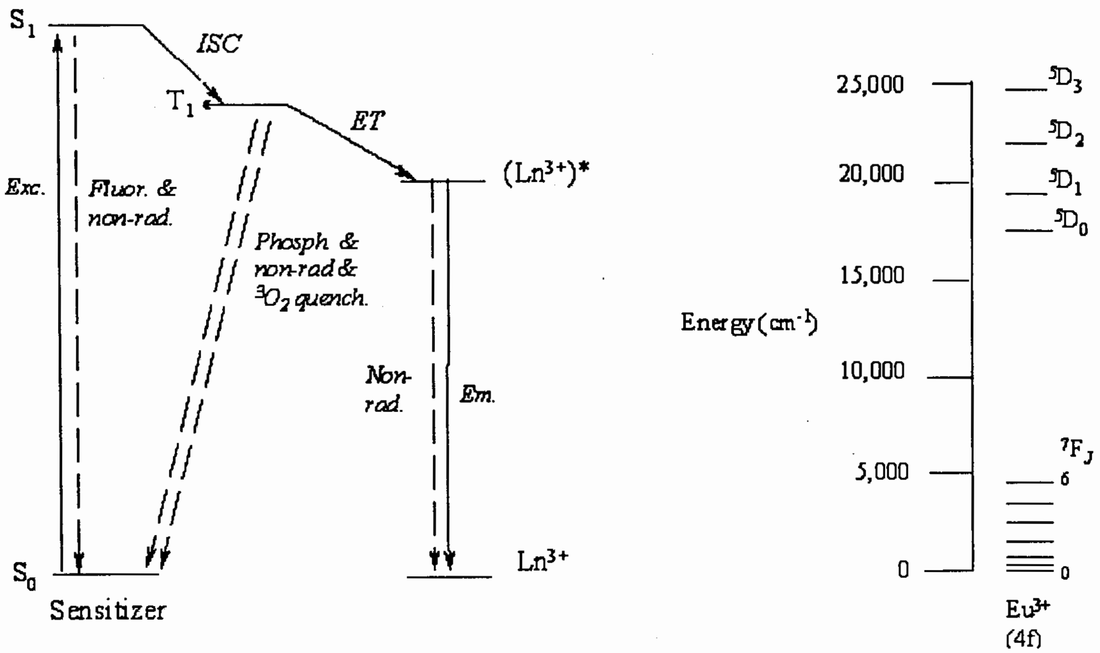

Figure 1.3: Left: schematic diagram of the photophysical pathway of the sensitization process. The solid arrows indicate sensitization process, and the dashed arrows indicate competing processes. Right: the relevant energy levels of Eu^{3+}. [24]

1.3.1 Development of water-soluble Ln^{3+} chelates

At present, there are three major kinds of water soluble chelators of rare earth ions: β-diketonate, phenanthroline, and salicylic acid derivatives. Historically, the first complexes reported were based on hydrophobic β-diketonates,[12] which forms 3:1 complexes, which are neutral overall.[13] Work done by Werts et al.[14] found that the high luminescent efficiency of Eu^{3+} complexes with β-diketonates is due to the luminescent pathway in the β-diketonates, which is more competitive with respect to non-radiative deactivation of the excited state. However, a complication arises from that fact that different lanthanides may need different chelating environments (Figure 1.4), depending on sensitivity to luminescent quenching[8] and the medium required for the application.

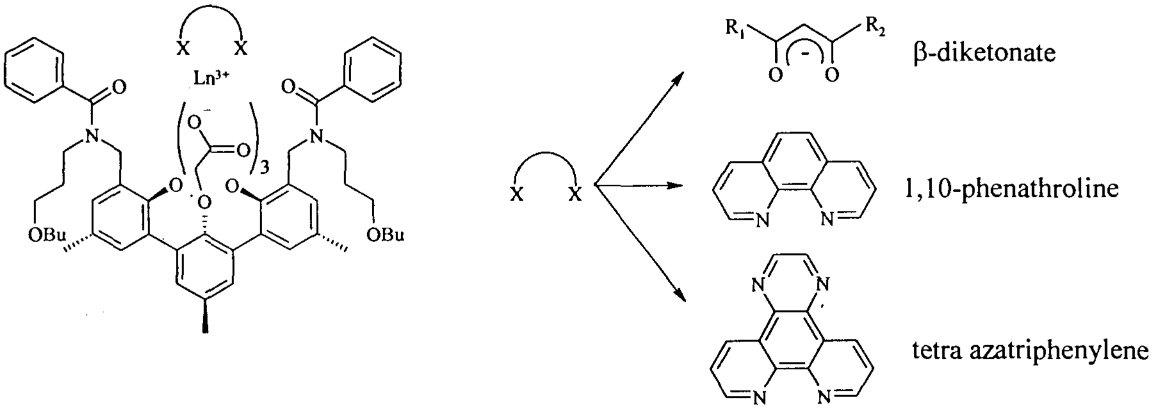

Figure 1.4: Schematic diagram of a polydentate m-terphenyl-based ligand for Ln^{3+} complexing. [24]

1.3.2 Development of water-soluble β-diketonate-based ligands

Ci et al.[15] and Matsumoto et al.[16] have developed water-soluble β-diketonate-based ligands; 5-chlorosulfonyl-2-thenoyltrifluoroacetone (CTTA) and 4,4'-bis(1",1",1",2",2",3",3"-heptafluoro-4",6"-hexanedion-6"-yl)chlorosulfo-*o*-terphenyl (BHHCT) respectively (Figure 1.5). The ligands were attached to a solid phase-bound biological macromolecule by conventional coupling procedures via the -SO_2Cl group of the ligand and the amino groups of the protein, producing a -SO_2-NH- linkage. Subsequently, the labeled macromolecules were transferred into solution with sodium dodecylsulfate, $EuCl_3$ and tri-n-octylphosphine oxide, and quantified using time-resolved fluorescent techniques (TR-FIA).

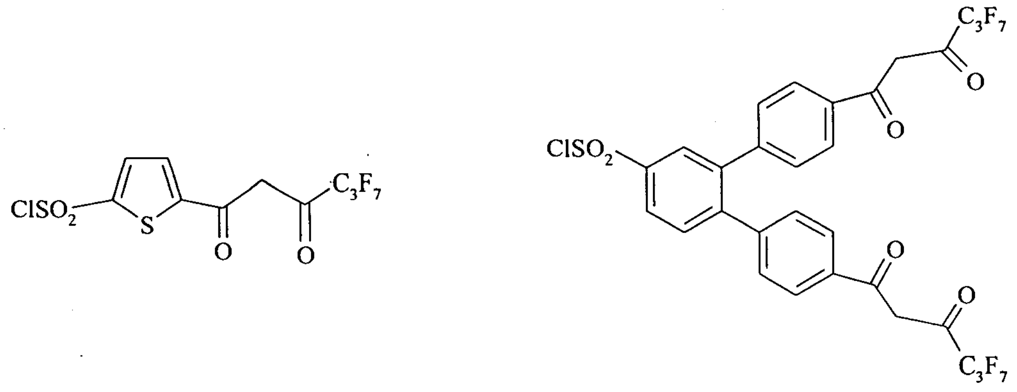

(CTTA)

(BHHCT)

Figure 1.5: Schematic representation of the water-soluble CTTA and BHHCT ligands.

The final results for the CTTA-Eu^{3+} complex gave a detection limit of 0.5 ng/ml, for cortisol, which was not a large improvement over already existing methods, mainly due to the low stability of the complex in solution. In contrast, the BHHCT-Eu^{3+} complexes yielded a detection limit of 6.5×10^{-2} pg/ml, which corresponded to 4 orders of magnitude increase compared to conventional immuno-assays for α-fetoprotein (AFP). One of the advantages of the BHHCT ligand is that it is a tetradentate ligand, resulting in a more stable complex formation compared to conventional bidentate ligands such as CTTA.

1.3.3 Development of water-soluble phenanthroline-based ligands

Several different variations of phenanthroline derivatives have been synthesized over the years, which have been designed for water solubility and potential use as a chelating ligand for fluorescent labels. Work done by Diamandis et al.[17] have developed a series of phenanthroline derivatives based on 4,7-bis(chlorosulfophenyl)-1,10-phenanthroline-2,9-dicarboxylic acid) (BCPDA), as shown in Figure 1.6. The ligand acts as an excellent chelator for Eu^{3+} ions with very strong fluorescent properties, and labels conjugates of streptavidin (SA) and thyroglobulin (TA) with minimized fluorescent quenching.

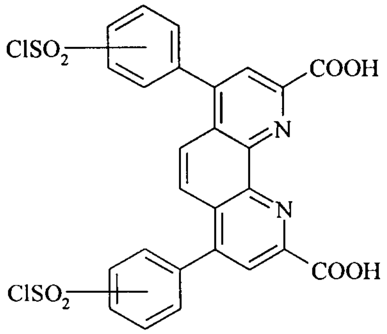

BCPDA

Figure 1.6: Schematic representation of the water-soluble BCPDA ligand.

Later work incorporated the BCPDA chelates into poly(vinyl amine) (PVA) and successfully attached biotinylated detection reagents (e.g.: antibodies), resulting in a multiple labeling technique that provided signal amplification with the ability to measure the fluorescence directly from the solid phase.[18] The advantage of this method is that it minimizes interaction with Eu^{3+}-related contaminated surfaces, such as dust or skin, due to the multiple transfer steps required for most immunoassays.[19]

1.3.4 Development of water-soluble salicylic acid-based ligands

Work using salicylic acid derivatives such as diethylenetriaminepentaacetic acid (DTPA) with 4-aminosalycilic acid (SA) ligands, shown in Figure 1.7, have been used to form chelates for immunoassay analysis. A large amount of label (few hundred moles of chelates per mole of analyte) was conjugated to a protein, resulting in a reported detection limit for human albumin (model analyte) of 10 mg/L, which is 100 fold lower than that for the single label system.[20]

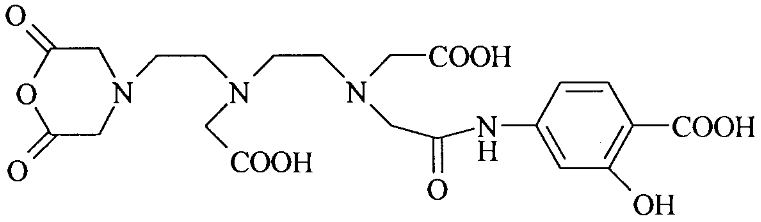

DTPA-SA derivative

Figure 1.7: Schematic representation of the water-soluble DTPA-SA derivative ligand.

1.3.5 Development of other water-soluble ligands

1.3.5.1 Azatriphenylene derivatives

Work done by Bakker et al.[9] has developed azatriphenylene-type antenna ligands for sensitized emission. Some of the advantages of the ligand are that the azatriphenylene π-system displays a long wavelength absorption (appreciable molar extinction coefficient of these compounds at $\lambda > 330$ nm),[21] a triplet state that is generated with high efficiency ($\Phi_{ISC} = 0.89$),[21] and features a very small energy gap between the lowest π-π*singlet and triplet states ($\Delta E = 6500$ cm^{-1}),[21] resulting in very fast and essentially irreversible energy transfer to the lanthanide ion. However, due to the inherent insolubility of many azatriphenylene-based ligands, the addition of carboxylate groups was carried out to render the complexes water soluble, as shown in Figure 1.8.

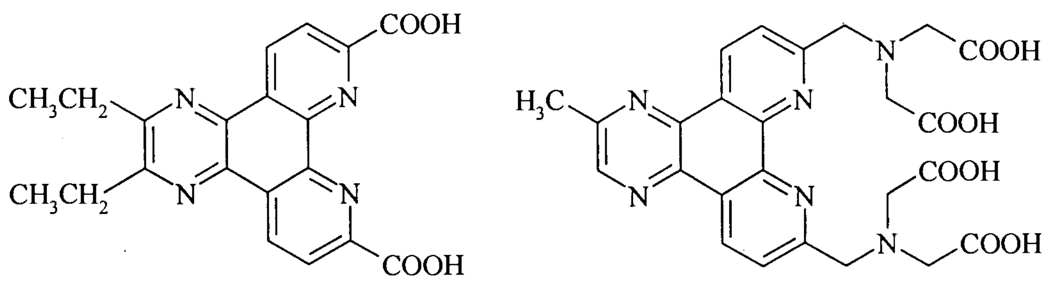

TATP-DC

TATP-TC

Figure 1.8: Schematic diagram of the ligands TATP-DC and TATP-TC.

The TATP-DC complex yielded a monoexponential luminescent lifetime of ~ 0.4 ms and a quantum yield of 17%, for Eu^{3+} and Tb^{3+} related complexes, which was dependent on whether the complex was in a 1:1 or 1:2 ratio, which affects the level of luminescent quenching by coordinated waters.

1.3.5.2 Fluorescein derivatives

Work done by Werts et al. [22] developed water-soluble fluorexon-based ligands for the sensitization of near-infrared (NIR) (750-2400 nm) emitting lanthanide ions (Nd^{3+}, Er^{3+} and Yb^{3+}). Previous work utilized AMFLU-DTPA and AMEO-DTPA ligands[23] (Figure 1.9) to complex the above lanthanide ions, however it was found that the energy transfer from the chromophore wasn't fast enough to compete with the quenching effects of dissolved molecular oxygen, which acts as an alternate acceptor of triplet energy, as demonstrated by the observed phosphorescence of $^1O_2^*$ at 1276 nm. Furthermore, incomplete ISC resulted in considerable amounts of the excitation energy being lost due to fluorescence of the chromophoric ligand.

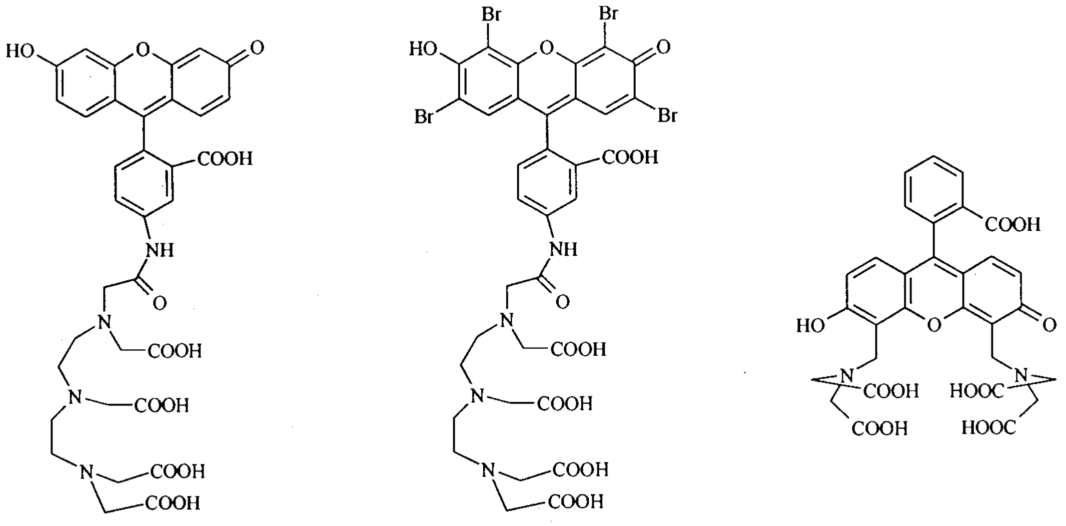

AMFLU-DTPA AMEO-DTPA Fluorexon

Figure 1.9: Schematic representation of the water-soluble fluorescein-based (AMFLU-DTPA)and Eosin-based (AMEO-DTPA) and fluorescein-based (Fluorexon) ligands.

Consequently, fluorexon-based ligands were developed, such that the binding site of the lanthanide ion in these complexes is significantly closer to the chromophore, as compared the AMFLU/AMEO-DTPA ligands. This allowed for a greater sensitization efficiency due to enhanced ISC in the antenna chromophore,[24] and more rapid intracomplex energy transfer. The resulting measured luminescent lifetimes in H_2O were ≤ 10 μs, with estimated quantum yields of lanthanide luminescence all less than 1%, by means of comparing the observed luminescent lifetime with that of the radiative lifetime of the lanthanide ion.

1.3.5.3 Cage-like derivatives

Due to terbium and europium ions having nine coordination sites, not all chelates (for example, but not limited to bidentate systems) complete the coordination shell, allowing the incorporation of a solvent molecule to fill the ninth coordination site, which reduces the overall luminescent properties due to vibrational deactivation. Development in the field of supramolecular chemistry revealed that cage-like ligands, (cryptates, complexes of branched-macrocyclic ligands, and complexes of functionalized calixarenes), are capable of encapsulating lanthanide ions, giving rise to complexes that are stable in solution. In particular, some of the general advantages of cryptates is that they are characterized by high stability (kinetic and thermodynamic), slower exchange rates (versus bidentate ligands), and more efficient shielding of the ion from the environment.[11] Due to the similarities between the alkali cations and the trivalent lanthanide ions, many cryptates accommodate the ions without significant change to the cavity size.

One of the drawbacks of the some of the initial cryptate approaches were with regards to lanthanide ions; the approach compromised the chromophore-to-ion energy transfer methodology (compared to branched macrocyclic ligands), resulting in less efficient ligand-to-metal intramolecular energy transfer.[25] Later work by Alpha et al.[26] incorporated 2,2'-bipyridine (bpy) groups to increase the lanthanide ion luminescence.

1.4 Nanoparticle systems

Nanoparticles are crystalline clusters of a few hundred to a few thousand atoms which are confined to an overall size of a few nanometers. Due to their small size, much of their chemical and physical properties are dominated by their surfaces and not by their bulk volume. Many of the advantages that are expected from NP are improved quantum effects for quantum dots (QDs), surface scattering effects for gold and silver NPs, and luminescent efficiencies (for both QDs and lanthanide-based NPs) that are superior to organic fluorophores.[27] As a result, the sytems are becoming highly favoured for biological applications such as bioconjugation due to their physical and optical properties.[28]

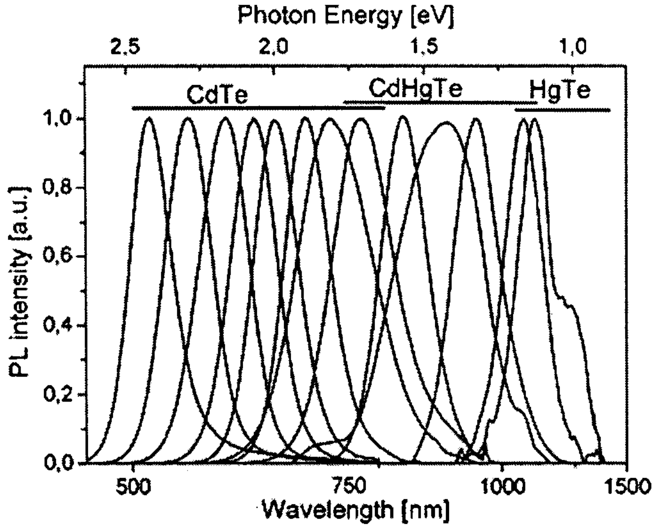

Figure 1.10: Schematic diagram of the spectral range of some quantum dots in which the emission lines extend into the NIR.[29]

At present, three types of NPs are commonly used in biological applications: latex nanospheres, luminescent quantum dots (QDs), and optically active metal NPs (such as gold or silver colloids).[30] Of the three, QDs have found significant use in biological applications, such as biological staining, diagnostics and fluorescence analysis, due to their high tunability of emission lines (Figure 1.10) and their well established synthetic protocols which imparts water-soluble properties.[31,32,33,34]

However, the development of water-soluble, lanthanide-based NPs is still an emerging field, in which expected advantages for potential biological applications are the non-overlapping absorption and emission lines that do not change position with particle size, and the inherent long-lived luminescent lifetimes (μs to ms range) that helps prevent interference from any spontaneous background emission sources (natural fluorescence of proteins are within 1-10 ns[32]). However, due to the inherent problem of luminescent deactivation by OH vibrational quenching pathways, the encapsulation of a large amount of luminescent lanthanide ions and/or chelates in one nanoparticle is being developed to overcome these problems.[35]

Work done by Härmä et al.[36,37,38] has capitalized on this approach by using carboxyl-modified polystyrene NPs (~107 nm) which are impregnated with Eu^{3+}- and Tb^{3+}-based chelates. The resulting NP contains about 30,000 chelates yielding very intense luminescence, with a luminescent lifetime of 720 μs (for Eu^{3+}), rivalling the chelates used in traditional dissociation enhanced fluoroimmunoassy (DELFIA) methods.[36] The NPs were used in NP-antibody binding conjugate binding studies with biotinylated prostate specific antigens (PSA), which was later extended to thyroid-stimulating hormone immunoassays and nucleic acid (NA) assays. In particular, the NA assays developed yielded a 100-1000 fold improvement in the sensitivity in relation to the reference Eu(III) chelate-labeled detection probes, as a result of increase of the luminescent lifetime of the NPs and the signal increase generated by the NP, instead of relying on target amplification (ie: increasing the number of targets to increase the number of luminescent chelates per area).

Other areas of NP development include functionalizing europium oxide NPs (300-600 nm in diamter) with 3-aminopropyltrimethoxysilane (APTMS) to form a hydrophilic layer of $O\text{-}Si\text{-}(CH_2)_3\text{-}NH_2$; this allows the NP to be labeled with amine-reactive targets, while the Si surface helps increase biocompatibility.[39] Utilizing these NPs with ELISA methodology for atrazine hapten immunoassays, a detection limit of 0.5 ng/ml was achieved, which compares to the detection limit of 0.1 ng/ml without optimizing the ELISA procedure.

Developments by Yuan et al.[40,41] has synthesized silica-coated Tb(III) chelate fluorescent NPs for TR-FIA applications. The NPs combine the advantages of both luminophore-doped silica NPs and the lanthanide latex fluorescence; smaller size (< 50 nm), high hydrophobicity, increased bio-compatibility (compared to free Tb^{3+} chelate), increased photostability and improved signal-to-noise ratio for TR-FIA due to the increase in luminescent lifetime (1.5 ms).

Other lanthanide-oxide NP systems include YVO_4-based NPs (~ 30 nm in diameter) doped with Eu^{3+} (at 20% doping level) that are synthesized directly in water by functionalizing with guanidinium groups, as shown in Figure 1.11.[42] In principle, the luminescent lanthanide ions are shielded from solvent-quenching effects by doping it in the inorganic VO_4^{3-} core of the NP, and capping the NP with an organic layer. The resulting NPs have measured quantum yields up to 20% for both excitation in the vanadate matrix or the 466 nm energy level of Eu^{3+}. The advantage of the above matrix is that the europium ion can be excited via energy transfer from the vanadate group

(VO_4^{3-}), at wavelengths below 350 nm due to the large absorption coefficient ($\alpha_{280\ nm}$) of 120,000 cm^{-1}, as compared to ($\alpha_{466\ nm}$) 3.3 cm^{-1} for Eu^{3+}.[42] Furthermore, one of the major advantages of the above system over chelate-based NPs is that they are highly resilient to photobleaching; they do not rely on carbon-carbon bonds for energy absorption and transfer which are susceptible to photodecomposition under intense irradiating light (ie: lasers).

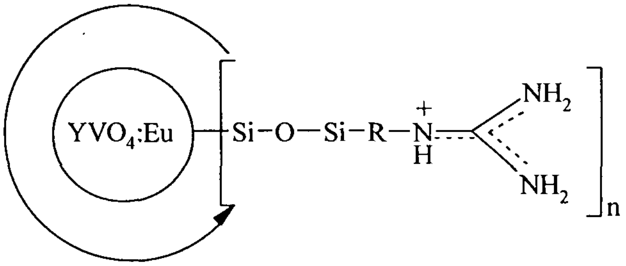

Figure 1.11: Schematic diagram of YVO_4*:Eu NPs, where the arrow represents that the silane-guanadinium stabilizing ligand is coated over the entire NP.*

Another approach is to make water-soluble, LaF_3-doped NPs, which also follows the ion-doping methodology discussed above, as shown in Figure 1.12. Though other variations of water-soluble NPs have used YVO_4-[42] and LaF_3-based matrices,[14] the LaF_3 matrix has the benefit of having the lowest phonon energy (350 cm^{-1}), which in principle leads to longer luminescent lifetime due to minimal vibrational quenching from the host material.[44] Water solubility of the NPs is achieved by coating the surface with an organic ligand, which in principle carries out three functions. The first is to minimize particle growth to the nanometer scale (< 50 nm), second, to stabilize the NP in solution to prevent particle breakdown, and third, to reduce the formation of surface-quenching sites on the NP. Furthermore, the luminescent lifetimes and quantum yields are expected to be larger than for complex-based NPs, because the luminescence of the LaF_3-doped NPs is not via sensitized emission, but by direct excitation of the ion itself, and therefore avoids the problems of energy loss due to intersystem-crossing and energy transfer processes.

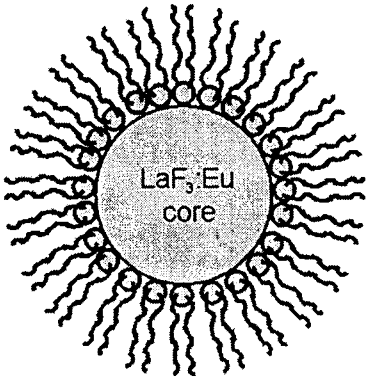

Figure 1.12: Schematic diagram of a LaF_3-doped NP, stabilized with organic ligands.

Though the development of water-soluble LaF_3-doped NPs, stabilized with citric acid showed strong Eu^{3+} luminescence,[14] for certain biological application needs such as bioconjugation, the carboxyl-terminated surface does not offer the ability to attach common heterobifunctional cross-linkers to the NP, without first modifying the NP surface. Work by Alexandrou et al.[42] with YVO_4-doped NPs (vide supra), whose particles could label sodium channels, required controlled polymerization of an alkoxysilane at the surface of the NP, followed by the addition of guanidinium groups on the surface.

Ultimately, the advantage of the LaF_3-based NP over other existing NP systems is through the ease of NP synthesis in aqueous environments at low temperatures (< 100 °C): addition of the lanthanide ions to a solution containing the desired ligand, produces NP whose average size is less than 20 nm. This procedure allows the spectroscopic selectivity of the NPs to be extended beyond the range of interferences from biological systems, by means of doping with Er^{3+}, Nd^{3+}, Pr^{3+}, or Ho^{3+} for near-infrared (NIR) emission lines.[43,44,45,46] This is important due to recent developments of biological imaging techniques,[29,47,48] *in situ* and *in vivo*, that have emerged where the effects of absorption (water, haemoglobin and various tissue) and scatter (variations in skin tissue density)[49] are minimized. Theoretical modeling studies by Gao et al.[48] indicate that two spectral windows are available for in vivo imaging; one from 700-900 nm and the other from 1200-1600 nm, both being in the NIR range. Additionally, the method offers a single-step procedure that stabilizes NPs with a ligand that can be attached directly to a cross-linking compound, without the need to carry out any preliminary surface modification for biological applications.

1.5 Summary

This chapter was designed to review the basic theory behind lanthanide luminescence, and some of the factors that influence it. Initial development of sensitized emission via chromophoric ligands resulted in superior luminescence over that of the free ion in solution. However, with the advances in biological areas of research, the utility of lanthanide ions is significant due to several properties: photostability, ability to be incorporated into water-soluble matrices, array of emission lines ranging from the visible to the NIR, and their long-lived luminescent lifetimes. Consequently, these lanthanide-based systems are ideal for time resolved applications, as already commercialized with DELFIA and other immunoassay techniques. The next chapter will cover the developments in bioconjugation chemistry and how it has allowed the incorporation of luminescent probes, ranging from chelates to NPs, to be utilized in potential biological diagnostic applications.

1.6 References

[1] G. Stein, E. Würzberg (1975) *J. Chem. Phys.* **62**, 208-213.

[2] G.K. Liu, X.Y. Chen, N.M. Edelstein, M. F. Reid, J. Huang (2004) *J. Alloys and Compounds* **374**, 240-244.

[3] J.H. Kim, P.H. Holloway (2005) *Adv. Mater.* **17**, 91-96.

[4] K.A. Gschneidner, L. Eyring (eds.), *Handbook on the Physics and Chemistry of Rare Earths*, vol. 25, Elsevier (1998).

[5] G. F. de Sá, O. L. Malta, C. de Mello Donegá, A. M. Simas, R. L. Longo, P. A. Santa-Cruz, E. F. da Silva Jr. (2000) *Coord. Chem. Rev.* **196**, 165-195.

[6] H. Peng, H. Song, B. Chen, S. Lu,S. Huang (2003) *Chem. Phys. Lett.* **370**, 485-489.

[7] Z. Wei-Wei, X. Mei, Z. Wei-Ping, Y. Min, Q. Ze-Ming, X. Shang-Da, C. Garapon (2003) *Chem. Phys. Lett.* **376**, 318-323.

[8] M.H.V. Werts, R.T.F. Jukes and J.W. Verhoeven (2002) *Phys. Chem. Chem. Phys.* **4**, 1542-1548.

[9] B.H. Bakker, M. Goes, N. Hoebe, H.J. van Ramesdonk, J.W. Verhoeven, M.H.V. Werts, J.W. Hofstraat (2000) *Coord. Chem. Rev.* **208**, 3-16.

[10] M.P. Oude Wolbers, F.C.J.M. van Veggel, B.H.M. Snellink-Ruël, J. W. Hofstraat, F.A.J. Guerts, D.N. Reinhoudt (1998) *J. Chem. Soc. Perkin Trans. 2*, 2141-2150.

[11] K.A. Gschneidner, L. Eyring (eds.), *Handbook on the Physics and Chemistry of Rare Earths*, vol. 23, Elsevier (1996).

[12] L.R. Melby, N.J. Rose, E. Abramson, J.C. Caris (1964) *J. Am. Chem. Soc.* **86**, 5125-5131.

[13] G. Hebbink, *Luminescent Materials based on Lanthanide Ions*, Ph.D. thesis, Twente University Press, 2002.

[14] V. Sudarsan, F.C.J.M. van Veggel , R.A. Herring, M. Raudsepp (2005) *J. Chem. Mater.* **15**, 1332-1342.

[15] X-D. Yang, Y-X. Ci, W-B. Chang (1994) *Anal. Chem.* **66**, 2590-2594.

[16] J. Yuan, K. Matsumoto (1998) *Anal. Chem.* **70**, 596-601.

[17] E.P. Diamandis, R.C. Morton, E. Rerichstein, M.J. Khosravi (1989) *Anal. Chem.* **61**, 48-53.

[18] A. Scorilas, A. Bjartell, H. Lilja, C. Moller, E.P. Diamandis (2000) *Clin. Chem.* **46**, 1450-1455.

[19] R.C. Morton, E.P. Diamandis (1990) *Anal. Chem.* **62**, 1841-1845.

[20] C. Sun, J. Yang, L. Li, X. Wu, Y. Liu, S. Liu (2004) *J. Chromatogr. B* **803**, 173-190.

[21] E.B van der Tol, H.J. van Ramesdonk, J.W. Verhoeven, F.J. Steemers, E.G. Kerver, W. Willem and D.N. Reinhoudt (1998) *Chem. Eur. J.* **4**, 2315-2323.

[22] M.H.V. Werts, J.W. Verhoeven, J.W. Hofstraat (2000) *J. Chem. Soc., Perkin Trans. 2* **3**, 433-439.

[23] M.H.V. Werts, J.W. Hofstraat, F.A.J. Geurts, J.W. Verhoeven (1997) *Chem. Phys. Lett.* **276**, 196-201.

[24] S.I. Klink, G.A. Hebbink, L. Grave, P.G.B. Oude Alink, F.C.J.M. van Veggel, and M.H.V. Werts (2002) *J. Phys. Chem. A* **106**, 3681-3689.

[25] C. Galaup, J. Azema, P. Tisnes, C. Picard, P. Ramos, O. Juanes, E. Brunet, J.C. Rordiguez-Ubis (2002) *Helv.Chim. Acta* **85**, 1613-1625.

[26] B.Alpha, J-M. Lehn, G. Mathis (1987) *Angew. Chem. Int. Ed. Engl.* **26**, 266-267.

[27] Z. Ye, M. Tan, G. Wang and J. Yuan (2004), *J. Mater. Chem.* **14**, 81-856.

[28] X. Hai, M. Tan, G. Wang, Z. Ye, J. Yuan, K. Matsumoto (2004) *Anal. Sci.* **20**, 245-246.

[29] N. Gaponik, I.L. Radtchenko, M.R. Gerstenberger, Y.A. Fedutik, G.B. Sukhorukov, A.L. Rogach (2003) *Nano. Lett.* **3**, 369-372.

[30] C. Sun, J. Yang, L.Li, X. Wu, Y. Liu, S.Liu (2004) *J. Chromatogr. B* **803**, 173-190.

[31] J.M. Tsay, M. Pflughoefft, L.A. Bentolila, S. Weiss (2004) *J. Am. Chem. Soc.* **126**, 1926-1927.

[32] M. Tan, Z. Ye, G. Wang and J. Yuan (2004) *Chem. Mater.* **16**, 2494-2498.

[33] Z. F. Li, E. Ruckenstein (2004) *Nano Lett.* ***8***, 1463-1467.

[34] D. Wang, A. L. Rogach and F. Caruso (2002) *Nano Lett.* **8**, 857-861

[35] T. Steinkamp, U. Karst (2004) *Anal. Bioanal. Chem.* **380**, 24-30.

[36] T. Soukka, H. Härmä, J. Paukkunen, T. Lövgren (2001) *Anal. Chem.* **73**, 2254-2260.

[37] A-M. Pelkkikangas, S. Jaakohuta, T. Lövgren, H. Härmä (2004) *Anal. Chim. Acta* **517**, 169-176.

[38] P. Huhtinen, J. Vaarno, T. Soukka, T. Lövgren, H. Härmä (2004) *Nanotechnol.* **15**, 1708-1715.

[39] J. Feng, G. shan, A. Maquieira, M.E. Koivunen, B. Guo, B.D. Hammock, I.M. Kennedy (2003) *Anal. Chem.* **75**, 5282-5286.

[40] Z. Ye, M. Tan, G. Wang, J. Yuan (2004) *Anal. Chem.* **76**, 513-518.

[41] M. Tan, G. Wang, X. Hai, Z. Ye, J. Yuan (2004) *J. Chem. Mater.* **14**, 2896-2901.

[42] E. Beaurepaire, V. Buisette, M-P.Sauviat, D. Giaume, K. Lahlil, A. Mercuri, D. Casanova, A. Huignard, J-L. Martin, T. Gacoin, J-P. Boilot, A. Alexandrou (2004) *Nano Lett.* **4**, 2079-2083.

[43] G. A. Hebbink, J.W. Stouwdam, D.N. Reinhoudt, F.C.J.M. van Veggel (2002) *Adv. Mater.* **16**, 1147-1150

[44] J.W. Stouwdam and F.C.J.M. van Veggel (2002) *Nano Lett.* **7**, 733-737

[45] K. Driesen, R.van Deun, C. Görller-Walrand, K. Binnemans (2004) *Chem. Mater.* **16**, 1531-1535

[46] J.W. Stouwdam, G.A. Hebbink, J. Huskens, F.C.J.M. van Veggel (2003) *Chem. Mater.* **15**, 4604-4616.

[47] Y.T. Lim, S. Kim, A. Nakayama, N.E. Stott, M.G. Bawendi, J.V. Frangioni (2003) *Mol. Imaging* **2**, 50-64.

[48] X. Gao, Y. Cui, R.M. Levenson, L.W.K. Chung, S. Nie (2004) *Nat. Biotechnol.* **22**, 969-976.

[49] G. Strangman, D.A. Boas, J.P. Sutton (2002) *Biol. Psychiatry* **52**, 679-693.

Chapter 2

Heterobifunctional Cross-Linkers for Bioconjugation Techniques

2.1 Introduction

The need for both structural elucidation and biological detection techniques require a system that can bind to an area of interest of a biological macromolecule, and signal its presence. Most naturally occurring chromophoric amino acids are inadequate for high through-put needs, as a result of short luminescent lifetimes, high susceptibility to quenching by the surrounding environment, and very low quantum yields.

The aromatic amino acids (AAAs) commonly found in most proteins are phenylalanine, tyrosine and tryptophan, each having a major absorption bands between 200-300 nm (257, 274, and 280 nm respectively), with a relative extinction coefficient ratio of 1:1:27 respectively (Figure 2.1).[1] As a result of the spectral distribution and relative extinction coefficients of the AAAs, tryptophan generally dominates the absorption, fluorescence, and phosphorescence spectra of proteins, regardless of whether the other two AAAs are present. The luminescent lifetimes of most AAAs at physiological conditions are within 3-4 ns, but tryptophan for example, at 77 K, has a quantum yield (Φ) of 0.17 when the measured phosphorescence lifetime is 6 s, and can quickly drop to a Φ value of $3\text{x}10^{-5}$ with a measured lifetime of 1 ms. Consequently, combined with the small Stoke's shift, the background luminescence (auto-fluorescence) of proteins is a significant drawback in proteins studies, even with gated-phosphorescence.[2] Therefore, the development of water soluble, luminescent probes, based on organic compounds, metal complexes (transition metal and rare earth ions), and nanoparticle (NP) methodologies have come to the fore front as an alternative method.

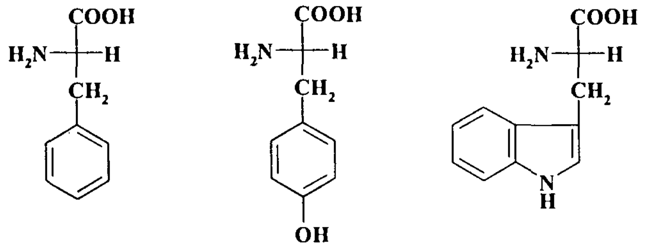

	Phenylalanine	**Tyrosine**	**Tryptophan**
λ_{ex}	257 nm	274 nm	280 nm
λ_{em}	282 nm	303 nm	348 nm
Φ_{avg}	0.04	0.14	0.20

Figure 2.1: Schematic diagram of the structures of three aromatic amino acids.

Proteins have at least two functional groups that can be derivatized in order to be attached to a probe: the amino and carboxyl group. Due to the reduced activity of the carboxylic group at the *C*-terminus, which must undergo derivatization first before being used, the amino group at the *N*-terminus is commonly used. Many different organic-based derivatizing agents for amino acids have been developed, such as 6-AQC in Figure 2.2.[3]

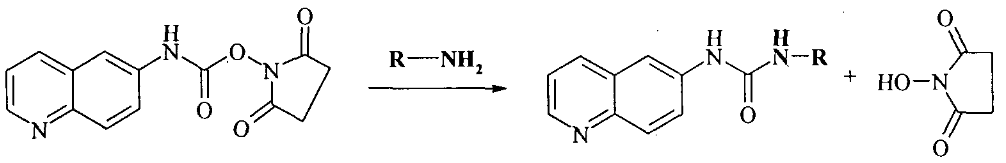

6-AQC

Figure 2.2: Schematic diagram of the reaction of 6-ACQ with a primary amine-bearing compound.

The 6-ACQ structure is designed to react with primary and secondary amino groups through its activated carbamate, which fluoresces strongly at 395 nm upon 250 nm excitation by light. Though it has a large Stoke's shift (> 100 nm), thereby minimizing background noise, the disadvantages is that its low excitation wavelength may damage proteins.

Other examples of organic compounds that have been used extensively are, among many others, fluorescein-5-isothiocyante (FTIC) and Alexa Fluor® dyes. Though highly fluorescent, problems with either water solubility, overall quantum yield or luminescent lifetimes of these organic probes have limited their use for high throughput analyses. Additionally, only a handful of organic dyes, such as cyanine, squarine and oxazine-based dyes (Figure 2.3),[3,4] can emit in the near infrared (NIR) (750-2400 nm), which is becoming an important consideration for biological imaging applications.[5]

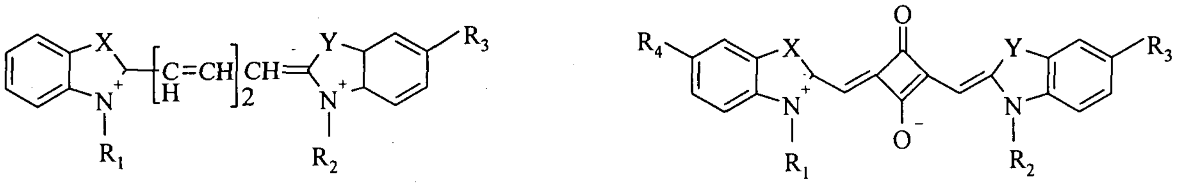

dicarbocyanine dye

symmetrical squarine

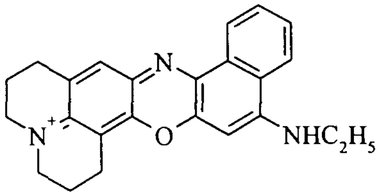

oxazine 750

Figure 2.3: Schematic diagram of some NIR emitting dyes

Of the many different commercially available immunoassay (IA) methodologies that exist, such as fluorescence-IA, enzyme-IA, radio-IA, etc., dissociation enhanced lanthanide fluoroimmunoassay (DELFIA) technology is among the more popular and is based on the use of lanthanide chelate labels with unique fluorescent properties. Depending on the DELFIA application, ligands such as [*p*-(3,5-dichlorotriazinyl)benzyl]diethylenetriamine-N^1,N^2,N^3,N^3-tetraaacetic acid (N1) are used, in which the dichlorotriazinyl groups reacts with free amino groups on proteins forming a stable covalent bond (Figure 2.4).[6]

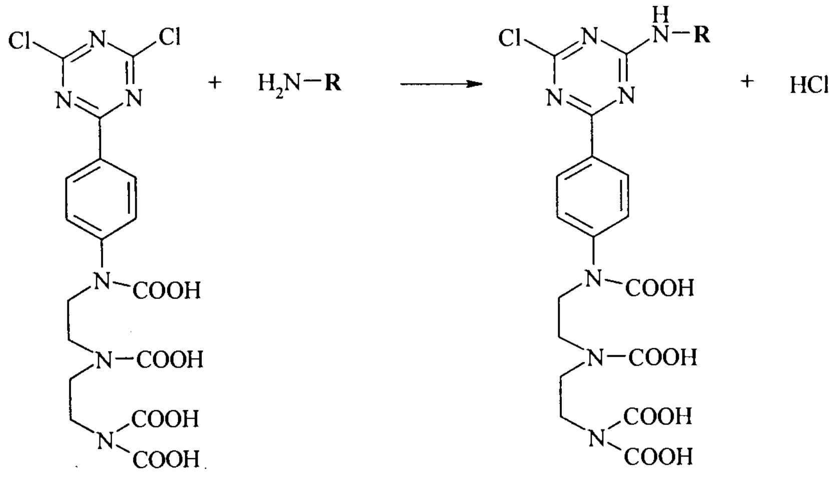

N1

Figure 2.4: Schematic diagram of N1 reacting with a primary amine-bearing compound.

The fluorescence lifetime of the (Ln^{3+})N1 ligand is several orders of magnitude longer than the non-specific background, and enables the label to be measured at a time when the background has already decayed (i.e.: gated-fluorescence). The combined large Stoke's shift and narrow emission peak contribute to increasing the signal-to-background noise ratio. Furthermore, the sensitivity of the method is increased because of the dissociation enhanced principle: subsequent to the lanthanide chelate binding to the target, the lanthanide ion is dissociated at low pH (< 4) and encapsulated in a protective micelle (enhancer solution) forming an even more highly fluorescent chelate, resulting in up to a 10^6 fold increase in fluorescence intensity.

However, despite these well established methodologies, many advantages are expected by replacing conventional molecular tags, such as fluorescent chromophores (both organic and complexed metal ions) with nanoparticles, including overall higher luminescent efficiencies, greater scatter for gold NPs, increased absorbance cross section for dyed polystyene beads, stronger luminescent intensity over more biocompatible wavelengths, and significantly increased chemical and photochemical stability.[7] To increase the versatility and utility of the luminescent probes, a variety of reagents has been developed that can label different functional groups on proteins, saccharides, nucleic acids, and other biological compounds, by means of cross-linking reagents.[23]

2.2 Cross-linking reagents

Cross-linking reagents are compounds bearing at least two reactive terminal groups, in which the appropriate functional groups may be used to link two entities where ideally, a hydrophilic, flexible, and biocompatible spacer such as poly(ethylene glycol) (PEG) is used (Figure 2.5).[8] Though cross-linking reagents are not luminescent themselves, they offer three main distinct advantages over traditionally used fluorophores for biological detection: (1) they permit protein immobilization on surfaces for increased isolation efficiency without affecting the protein activity, (2) they allows for facile attachment of highly fluorescent probes for increased signal intensity in relation to background signal (ideal for immunoassays), and (3) they are more widely applicable due to their versatility in end-group functionalization.

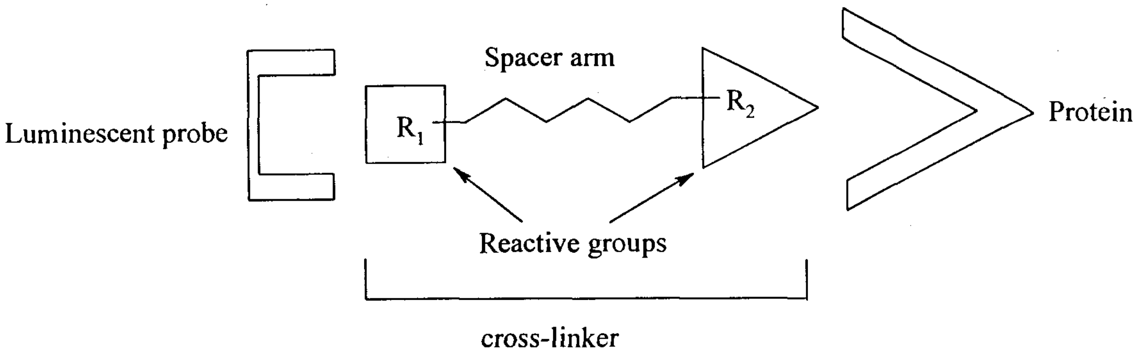

Figure 2.5: Schematic diagram of a cross-linker joining a protein with a luminescent probe.

Coupling reagents contain at least two reactive groups, and can be either homobifunctional (with two identical reactive groups) or hetero(multi)functional (with two or more different branched reactive groups).[8] Most homobifunctional cross-linkers react with primary amines which are commonly found on proteins, which have various reactive functional groups such as glutaraldehyde, imidates (-C-(C=NH)O-) and *N*-hydroxysuccinimidyl (NHS) esters. These cross-linkers are often used in a one-step reaction procedure in which the compounds to be coupled are mixed together, followed by the addition of the cross linker to the solution. Although this cross-linking method may result in self-conjugation, it may be the best choice if only primary amines are available. In particular, this method is more efficient for coupling with glutaraldehyde ($O=CH-(CH_2)_3-HC=O$) than with *N*-hydroxysuccinimide (NHS) esters because the latter is prone to hydrolysis. Otherwise, heterobifunctional cross-linkers (HBCs) are used when unacceptable levels of polymerization occur with homobifunctional reagents, for which a wide selection of HBCs are commercially available.[6]

Extensive work has been carried out using HBCs to link macromolecules to surfaces for needs of immunoassays, biosensors, or various probe applications.[9] Various functional groups have been developed that can label amino groups, thiols, imidazoles, phenols, carboxyls, hydroxyls,[10] aldehydes,[2] avidin, etc. Many of these HBCs come with, among others, a PEG spacer[11,12] for both water solubility and biocompatibility.

The unique ability for PEG to be soluble in both aqueous and organic solvents makes it suitable for end group derivatization and chemical conjugation to biological molecules under mild (physiological) conditions. From a biological standpoint, poly(ethylene glycol) (PEG) is rapidly cleared in vivo without structural change when the molecular weight is above 1000 Da (as noticed in the food, cosmetic and pharmaceutical industries), but below 400 Da, PEG chains are susceptible to degradation by enzymatic processes. PEG typically binds 2 - 3 water molecules per ethylene oxide unit and due to its highly flexible backbone, PEG molecules acts as if it were 5-10 times as large as a soluble protein of comparable molecular weight.

Additionally, solid phase support systems ranging from Si surfaces,[10,13] Nb_2O_5 surfaces,[14] and cross-linked agarose beads,[15] use PEG for its flexible spacer arm, minimal non-specific surface-binding properties, and its ability to minimize protein denaturing upon binding by not significantly affecting the molecular motion of the protein on the solid phase. In particular, the use of amine-, thiol-, carboxyl-, hydroxyl- and biotin-specific HBCs (Figure 2.6) have been used extensively due to their ability to derivatize molecules under physiological conditions.

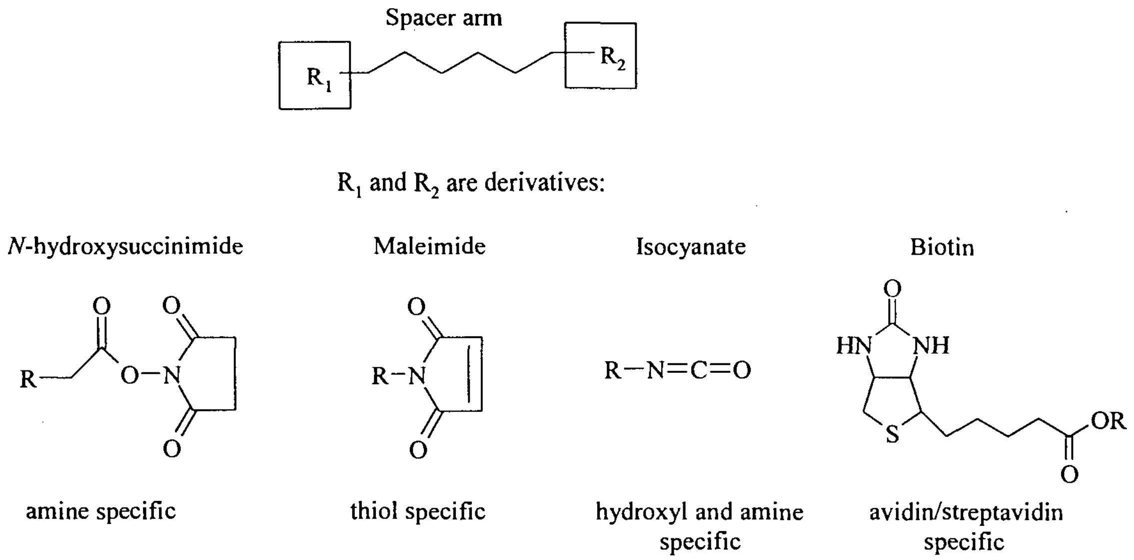

Figure 2.6: Schematic diagram of common functional groups used on HBCs.

2.2.1 Amine and thiol HBC

The majority of HBCs contain an amine-reactive functional group, as an NHS ester, with a second functional group that couples to different reactive substituents (thiols, avidin, etc.). The amine-reactive end of the cross-linker is typically an acylating agent possessing a good leaving group that can undergo nucleophilic substitution to form an amide bond with primary amines.[16] The NHS ester-HBC reactions are usually performed in two steps, with the NHS ester reaction performed first to minimize hydrolysis of the NHS ester functional group in aqueous solutions.

The thiol reactive portion, in contrast to the NHS ester, is usually an alkylating agent that is capable of creating a thioether linkage with thiol-containing molecules.[16] Many of the thiol-specific reagents such as maleimides, iodoacetimides, vinylsulfones and orthopyridyl disulfide were developed for cysteine (Cyst) modification (Figure 2.7), due to cysteine being one of the few naturally occurring amino acids present in a protein that contains a thiol.[8]

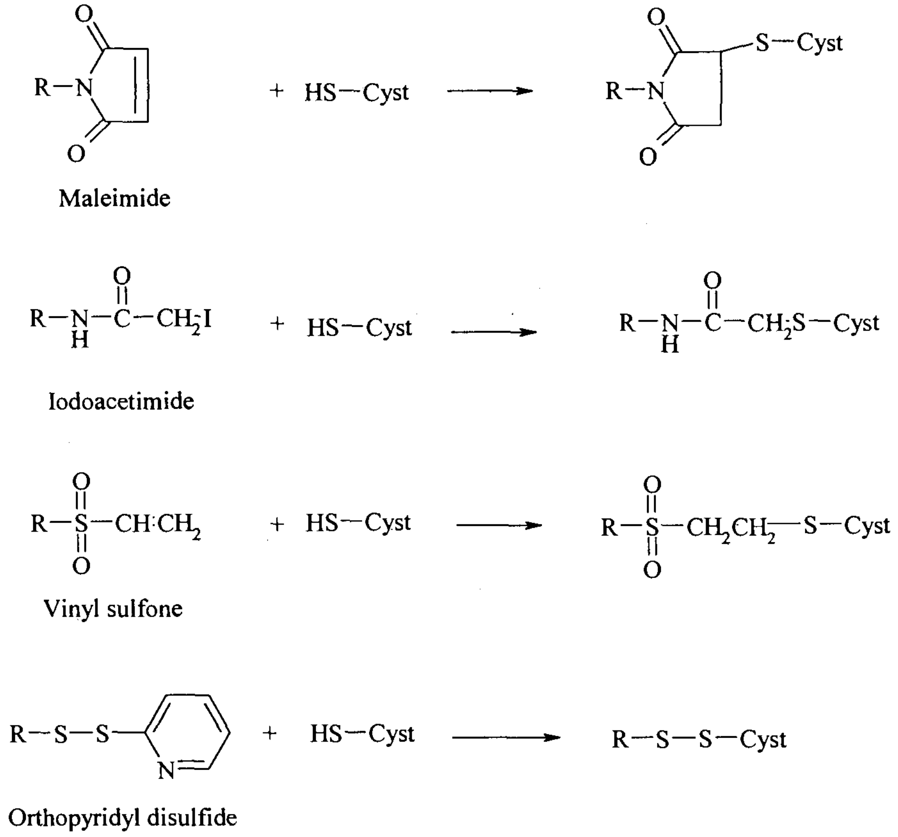

Figure 2.7: Schematic diagram of various thiol-reactive functional groups.[8]

In particular, the use of a maleimide group is common because it exhibits minimal non-specific reactions with other functional groups such as amines. Use of the maleimide unit takes advantage of its activated α,β-unsaturated double bond that reacts with thiols by means of a Michael addition. The thioether linkage formed between the maleimide unit and the protein, carried out in slightly acidic solutions (pH 6-7), is stable but slow cleavage of one of the amide linkages might occur by hydrolysis from the NHS unit.

If an enzyme contains free sulfhydryls on its surface, it can be conjugated to proteins using a two-step reaction procedure with an NHS ester-maleimide cross-linker (Figure 2.8). Traditionally, the NHS ester-maleimide HBCs are used to couple primary amines on proteins and introduce maleimide groups coupled to sulfhydryls on the second protein, forming stable, non-cleavable thioether bonds.

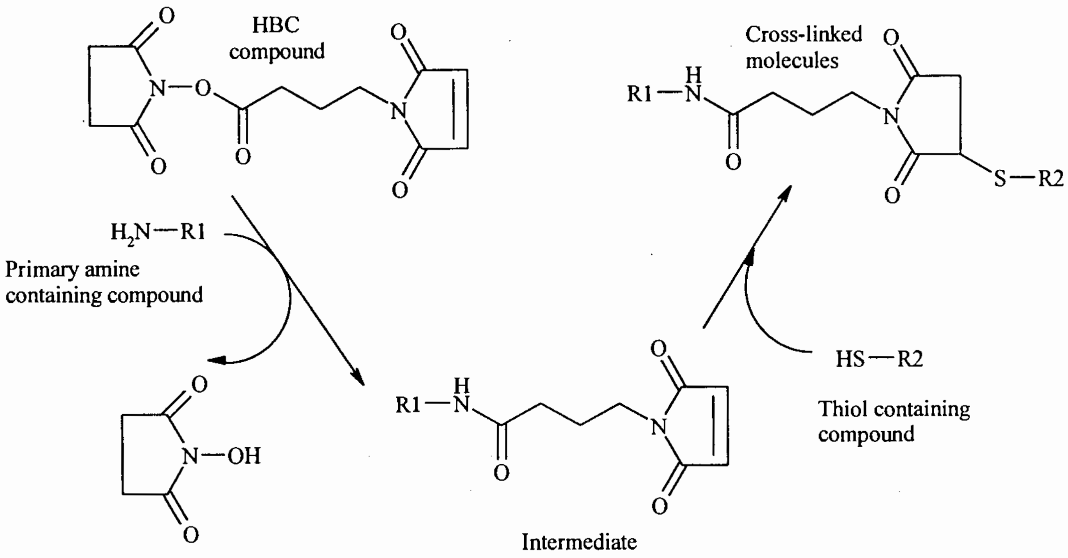

Figure 2.8: Schematic diagram of the process used in joining two moieties with an amine- and thiol-functionalized HBC.[16]

Manta et al.[15] have used this NHS-maleimide approach to bind β-amylase (29 lysine residues per subunit) to a thiopropyl-agarose solid support, where previous attempts with thiol-specific homobifunctional cross-linkers (PEG bis-oxirane) resulted in high levels of enzyme-enzyme cross-polymerization (CP). To reduce the effects of CP, NHS-PEG-maleimide HBC was used to cross-link the NHS unit with the primary amines on the surface of the enzyme, instead of thiol groups with the bis-oxirane. This resulted in the maleimide group of the HBC to react preferentially with the thiopropyl-susbstrate, due to the higher number of accessible thiol groups available for reaction than for the enzyme.

Other methods utilizing poly(*DL*-lactic acid) (PLA) NPs have converted the surface bound carboxyl groups to thiol groups through a carbodiimide reaction with cystamine, in which the disulfide bond was reduced with tris(2-carboxyethyl)-phosphine hydrochloride (TCEP).[17] The importance of converting the carboxyl group to a thiol, instead of an amine or NHS-ester, is the resulting ability to attach the PLA to neutravidin (avidin derivative) with an HBC; one end reacts with the amine site (neutravidin) and the other at the thiol site (PLA). As will be discussed below, though conversion of the carboxyl group to an amine-reactive ester is the more common route, using monobifunctional cross-linkers that are amine specific at both ends may potentially induce high levels of cross-polymerization within PLA and neutravidin units.

2.2.2 *Amine and carboxyl HBC*

Oxidation of carbohydrate residues is a technique commonly used that generates a reactive aldehyde group, which can be subsequently reacted with a hydrazide- or amine-functionalized compound, producing a hydrazone linkage or a reversible Schiff base, respectively. Addition of a strong reducing agent, such as $NaCNBH_3$, is necessary to reduce the double bond formed and stabilize the conjugate,[16] resulting in the formation of a zero-length cross-linker where no additional spacer atoms are introduced. This method is efficient for protein-to-protein conjugation because most proteins contain both primary amines and carboxyl groups; yet, the possibility of self-polymerization exists for the same reason. To circumvent the problem, the carboxyl groups are reacted with 1-ethyl-3(3-dimethylaminopropyl) carbodiimide hydrochloride (EDC) to form a urea derivative, which is subsequently reacted with NHS to form a stable activated ester for subsequent amine-specific reactions, as shown in Figure 2.9.

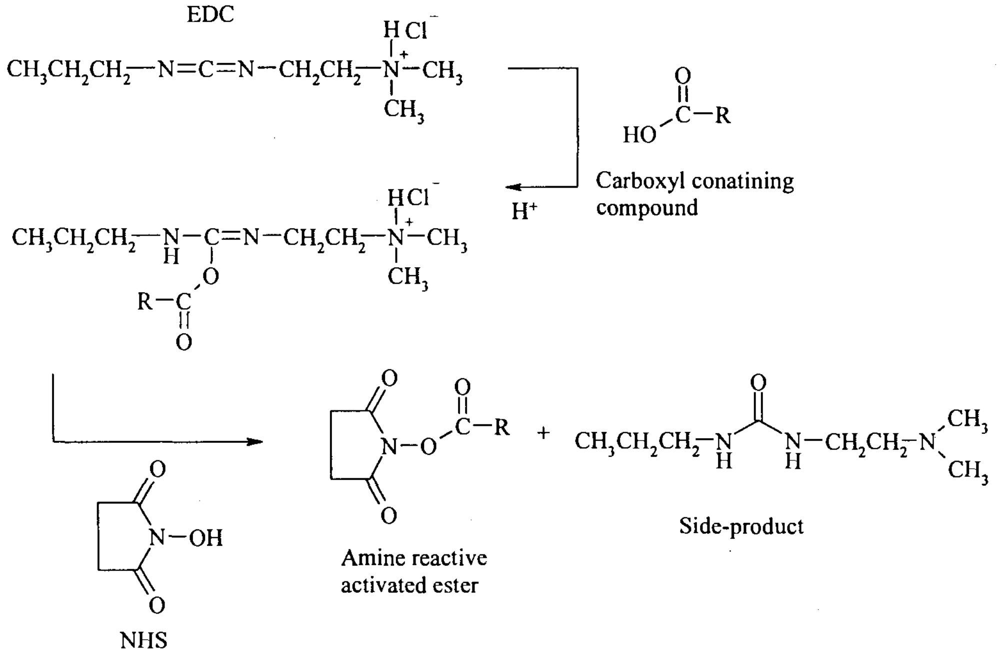

Figure 2.9: EDC-NHS derivatization reaction.

This procedure was used by Soukka et al.[18,19] to modify the surface of carboxyl terminated polystyrene NPs (107 nm) for covalent coupling of antibody systems. The NPs are impregnated with a europium(III) chelate and used in conjunction with DELFIA techniques for detection and quantification. One of the draw backs encountered with NP-based assays with DELFIA techniques is that it works under the assumption that the antibody density on the illuminated area is representative of the entire coated area, where as only about half of the NPs are actually coated. Other systems developed utilize gold NPs or CdTe QDs[20] terminated with carboxyl groups which are reacted directly with amine residues on proteins,[21] or were converted to NHS units for attachment of PEG and biotin-based PEG ligands for biotin-streptavidin binding.[22]

2.2.3 *Thiol and hydroxyl HBC*

Due to the increase in PEG usage for NP stabilization in high electrolytic solutions[22] and in coatings for solid phase support systems (SPS)[28], the use of hydroxyl-reactive HBCs is becoming more common instead of derivatizing PEG-based hydroxyl groups into another form that can react with commonly used HBCs. Cha et al.[10] have used *p*-maleimidophenyl isocyanate (PMPI) to link PEG molecules that were grafted onto Si surfaces in a brush-like configuration. The process involved the direct interaction of the HO-functinal group on the PEG with the isocyanate group to form a stable carbamate linkage (Figure 2.10). However, the disadvantages of the PMPI HBC are its very high sensitivity to moisture, rendering it too unstable for commercial sale, and its ability to react with amine-containing compounds.

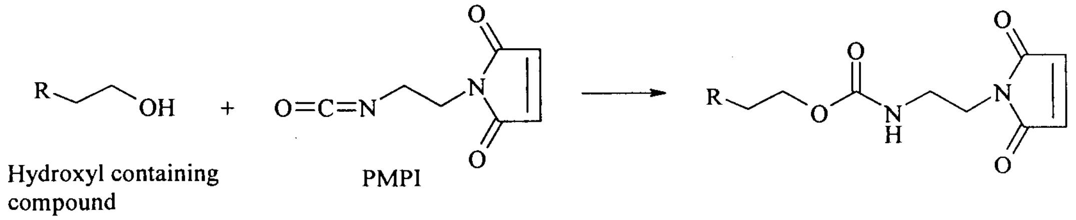

Figure 2.10: Schematic diagram of PMPI reacting with a hydroxyl-based compound.

2.2.4 *Amine and biotinylated HBC*

While other forms of HBCs exist that rely on the attachment techniques mentioned above, biotin-avidin (or streptavidin) binding is highly specific and irreversible under most ambient conditions, thus is the basis for the exploitation of avidin/ streptavidin as a HBC, in addition to usage in many biotechnological applications.[23]

Two of the most striking differences between avidin and streptavidin (SA) is in their respective isoelectric point (pI) values, and the fact that SA is not a glycoprotein (sugar-based compound). Avidin is strongly basic (pI≈10) since it is rich in arginine (eight/subunit, pK_a 12.5)[24] and lysine (nine/subunit, pK_a 10)[24] residues and is a glycoprotein (Figure 2.11).[25]

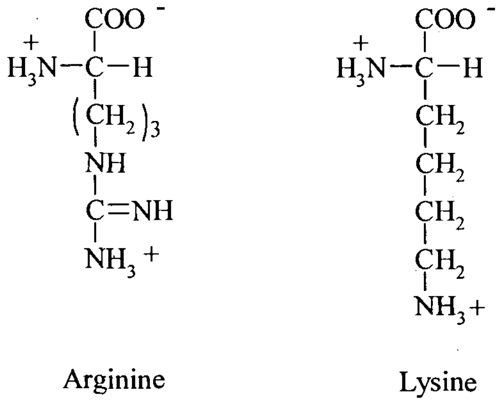

Figure 2.11: Schematic diagram of arginine and lysine, both bearing a predominantly positive charge at physiological conditions.

Consequently, the predominantly positive charge on the protein increases its tendency to react non-specifically with more negatively charged molecules, in addition to its tendency to bind to carbohydrate units on cells due the polysaccharide (sugar) portion of the avidin. In contrast, the low pI (5-6) for SA renders it neutral in solution due to its variation in amino acid sequence, which combined with the fact that it is not a glycoprotein, results in very low level of non-specific binding.[16] Despite the differences in sequence, the two proteins share similar tertiary and quaternary structure as well as a similar disposition of the relevant amino acids in the biotin-binding pocket.

A common application of avidin-biotin chemistry is in immunoassays: the specificity of antibody molecules provides the targeting capability to recognize and bind particular antigen molecules, especially if the antibody contains biotin labels. Though streptavidin has less non-specific binding properties, avidin-biotin has a higher affinity constant (K_a), thus is used fairly often [K_a (M^{-1}); avid-biotin: 10^{15}, SA-biotin: 10^{13}, antibody-antigen: 10^7-10^{11}].[26]

Research using biotinylated probes such as gold,[22] CdSe/ZnSe QDs[27] and SPS systems,[28,29] are commonly attached to avidin/streptavidin-coupled targets for ease of isolation and detection, and are often used as a proof-of-principle for potential bioconjugate systems. Though initial HBCs such as biotin-NHS were synthesized as short chained systems, steric hindrance often compromised the efficacy of the binding. This was later minimized by the addition of PEG spacer arms placed between the reactive termini (Figure 2.12). Biotin-NHS-based HBCs are widely used cross-linking systems with proteins, arising from the fact that lysine residues are numerous in most proteins, and characteristically occupy an exposed position rendering them ideal for NHS coupling. This, combined with the biotin-avidin binding properties, renders the system as an ideal method for protein isolation and sensing, where the avidin is bound to a SPS.

The development of biological detection systems for DNA, proteins, enzymes, etc., has typically taken the form of NP support or solid phase support procedures. Aslan et al.[22] have developed techniques where the immobilization of ligands on gold NPs (~ 20 nm diameter) by means of two-step process: (1) chemisorption of long-chained carboxyl-terminated alkane-thiol groups on gold NPs, and (2) covalent coupling of a heterobifunctional (amine and biotin) PEG-based ligands by means of NHS-EDC functionalization of the carboxyl groups. The procedure yielded stable, ligand-modified gold nanoparticles that exhibited interaction with streptavidin (SA), by means of biomolecular recognition, in which the PEG spacer, diethylene glycol to be specific, was used to increase NP solubility in aqueous environments, in addition to minimizing non-specific interactions with SA.

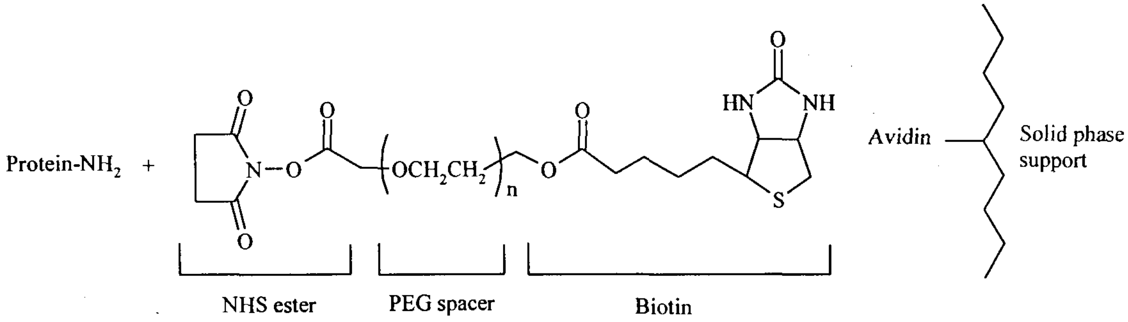

Figure 2.12: Schematic diagram of a biotin-PEG-NHS cross-linker. The NHS unit couples the amine-reactive portion of the protein, while the biotin unit binds to the avidin-functionalized surface.

2.3 Summary

The aim of this chapter is to give a brief overview of the different heterobifunctional cross-linkers available, and their various uses with different probing systems. Though many other forms do exist, ranging from other functional groups available for reaction to multi-branched cross-linkers (3 or more arms), the essence of the techniques used and possible variation of the cross-linkers is presented.

Though fluorescent probes have traditionally been limited to immunoassys, diagnostics, signal amplification, cross-linking studies, and affinity cytochemistry, the development of stable, highly luminescent, water-soluble NIR emitting NP probes has allowed them to expand into the field of biological imaging agents, which is becoming an area of interest due to the development of *in-vivo* imaging techniques. Here, NIR emitting quantum dots[30,31] are used for *in-vivo* studies of living tissue, which upon further studies will likely require the use of cross-linkers for site-specific attachment requirements.

2.4 References

[1] http://www.biotek.com

[2] J.R. Lakowicz (ed.), Topics in Fluorescence Spectroscopy: Biochemical Applications, Plenum Press (1992).

[3] C. Sun, J. Yang, L. Li, X. Wu, Y. Liu, S. Liu (2004) *J. Chromatogr. B* **803**, 173-190.

[4] M. Casalboni, F. De Matteis, P. Prosposito, A. Quatela, F. Sarcinelli (2003) *Chem. Phys. Lett.* **373**, 372-378.

[5] N. Gaponik, I.L. Radtchenko, M.R. Gerstenberger, Y.A. Redutik, G.B. Sukhorukov, A.L. Rogach (2003) *Nano Lett.* **3**, 369-372; M. Green (2004) *Angew. Chem. Int. Ed.* **43**, 4129-4131; S. Kim, T. Lim, E.G. Soltesz, A.M. De Grand, J. Lee, A. Nakayama, J.A. Parker, T. Mihaljevic, R.G. Laurence, D.M. Dor, L.H. Cohn, M.G. Bawendi, J.V. Frangioni (2004) *Nat. Biotechn.* **22**, 93-97.

[6] http://las.perkinelmer.com.

[7] H. Otsuka, Y. Nagasaki, K. Kataoka (2003) *Adv. Drug. Deliv. Rev.* **55**, 403-419.

[8] M.J. Roberts, M.D. Bently (2002) *Adv. Drug. Deliv. Rev*. **54,** 459-476.

[9] C. Jiarong, M. Yuquig, H. Nongyue, W. Xiaohua, L. Sijiao (2004) *Biotechn. Adv.* **22**, 505-518; D.P. O'Neal, L.R. Hirsch, N.J. Halas, J.D. Payne, J.L. West (2004) *Cancer Lett.* **209**, 171-176.

[10] T-W. Cha, V. Boiadjiev, J. Lozano, H. Yang, X-Y. Zhu (2002) *Anal. Biochem.* **311**, 27-32.

[11] C. Woghiren, B. Sharma S. Stein (1993) *Bioconjug. Chem.* **4**, 314-318; H.F. Gaertner, R.E. Offord (1996) *Bioconjug. Chem.* **7**, 38-44; Y. Akiyama, H. Otsuka, Y. Nagasaki, M. Kato, K. Kataoka (2000) *Bioconjug. Chem.* **11**, 947-950; S. Zhang, J. Du, R. Sun, X. Li, D. Yang, S. Zhang, C. Xiong, Y. Peng (2003) *React. Funct. Polym.* **56**, 17-25.

[12] F.M. Veronese (2001) *Biomat.* **22**, 405-417; M.J. Roberts and M.D. Bently (2002) *Adv. Drug. Deliv. Rev.* **54**, 459-476; H. Otsuka, Y. Nagasaki, K. Kataoka (2003) *Adv. Drug. Deliv. Rev.* **5**, 403-419.

[13] H. Otsuka, Y. Nagasaki, K. Kataoka (2004) *Langmuir* 20, 11285-11287.

[14] Y. Fang (2002) *J. Am. Chem. Soc.* **124**, 2394-2395.

[15] C. Manta, N. Ferraz, L. Betancor, G. Antunes, F. Batista-Viera, J. Carlsson, K. Caldwell (2003) *Enzyme Microb. Technol.* **33**, 890-898.

[16] G.T. Hermanson: Bioconjguate Techniques, Academic Press (1996).

[17] L. Nobs, F. Buchegger, R. Gurny, E. Allémann (2004) *Eur. J. Pharm. Biopharm.* **58**, 483-490.

[18] T. Soukka, K. Antonen, H. Härmä, A-M. Pelkkikangas, P. Huhtninen, T. Lövgren (2003) *Clin. Chem. Acta* **328**,45-58.

[19] A-M. Pelkkikangas, S. Jaakohuta, T. Lövgren, H. Härmä (2004) *Anal. Chim. Acta* **517**, 169-176.

[20] S. Wang, N. Mamedova, N.A. Kotov, W. Chen, J. Studer (2002) *Nano Lett.* **8**, 817-822.

[21] J. Henry, A. Anand, M. Chowdhury, G. Coté, R. Moreira, T. Good (2004) *Anal. Biochem.* **334**, 1-8

[22] K. Aslan, C.C. Luhrs, V.H. Perez-Luna (2004) *J. Phys. Chem B* **108**, 15631-15639.

[23] M. Wilchek, E.A. Bayer (eds.), Methods in Enzymology: Avidin-biotin technology, vol. 184 Academic Press (1990).

[24] http://www.agsci.ubc.ca/courses/fnh/410/protein.

[25] M. Morpurgo, A. Radu, E. A. Bayer, M. Wilchek (2004) *J. Mol. Recognit.* **17**, 558-566.

[26] M. Wilchek, E.A. Bayer (1999) *Biomol. Eng.* **16**, 1-4.

[27] N. Charvet, P. Reiss, A. Roget, A. Dupuis, D. Grünwald, S. Carayon, F. Chandezon, T. Livache (2004) *J. Mater. Chem.* **14**, 2638-2642.

[28] B. Städler, D. Falconnet, I. Pfieffer, F. HööK, J. Vörös (2004) *Langmuir* **20**, 11348-11354.

[29] A. Arakaki, S. Hideshima, T. Nakagawa, D. Niwa, T. Tanaka, T. Matsunaga, T. Osaka (2004) *Biotechnol. Bioeng.* **4**, 543-546.

[30] S. Kim, S. Kim, T. Lim, E.G. Soltesz, A.M. De Grand, J. Lee, A. Nakayama, J.A. Parker, T. Mihaljevic, R.G. Laurence, D.M. Dor, L.H. Cohn, M.G. Bawendi, J.V. Frangioni (2004) *Nat. Biotechn.* **22**, 93-97.

[31] X.Gao, Y. Cui, R.M. Levenson, L.W.K. Chung, S. Nie (2004) *Nat. Biotechnol.* **22**, 969-976.

Chapter 3

Synthesis of Water-Soluble Nanoparticles with Poly(ethylene glycol) and Amine-Terminated Ligands[1]

3.1 Introduction

Poly(ethylene glycol) (PEG) is a highly investigated polymer for the covalent modification of biological macromolecules and surfaces for many pharmaceutical and biotechnical applications. In particular, the modification of macromolecules, peptides and proteins by PEGylation (ie: the covalent attachment of PEG) allow for an increase circulating in half-life, solubility, and reduced immunogenicity.[1] Furthermore, due to its amphillic nature, use of PEG-based materials ranges from drug carriers, surface modifiers to colloidal dispersants.[2]

PEG offers three important aspects: (1) it increases solubility in aqueous environments; (2) it minimizes particle aggregation and/or agglomeration in the applied media, such as highly concentrated electrolyte solutions, and (3) it helps minimize non-specific interaction between the nanoparticles (NPs) and biological macromolecules (proteins and enzymes).[3] That is, many water-soluble NPs are based on charged ligands, so that upon immersion in highly concentrated electrolytic solutions (ie: buffer solution used to prevent denaturing of most proteins), the potential of NP aggregation may exist.

Zheng et al.[3] demonstrated by using different PEG chain lengths, ranging from 2 to 4 ethylene glycol units on 3.5 nm gold NPs, that they were found to be highly stable in

---

[1] The major part of the work in this chapter was accepted for publication: P.R. Diamente, F.C.J.M. van Veggel (2005) *J. Fluor.*.

aqueous environments, including solutions with a high electrolyte concentration. Furthermore, ion-exchange chromatography and gel electrophoresis showed that the NPs were free of any non-specific binding with various proteins, DNA, and RNA. Contrary to conventional use of long-chained PEG ligands commonly used in pharmaceutical applications (see Chapter 2), the application of short-chained ligands with a defined length can form more densely-packed monolayers on the surface of the NP. This results in increasing particle stability, minimizing the potential of non-radiative decay process due to surface-bound quenching sites, and increasing the potential binding sites on the surface of the NP. From there, the NP acts as a modular platform with which its surface can be subsequently modified with a variety of functionalized ligands for a given application.

The concept of a modular platform is utilized by many researchers. Work done by Aslan et al.[4] reported the synthesis of water-soluble gold NPs (~ 20 nm diameter) where surface modification of the terminal carboxyl groups, to active N-hydroxysuccinimide(NHS)-esters by means of routine NHS-EDC (EDC = 1-ethyl-3(3-dimethylaminopropyl) carbodiimide hydrochloride) reaction techniques, allows the coupling of a controlled amount of an amine-terminated ligand. Quantum dot (QD) systems by Kotov et al.[5] used CdTe NPs that were stabilized with L-cysteine for water-solubility properties, and were linked to bovine serum albumin (BSA) by means of glutaraldehyde coupling. The use of glutaraldehyde allows one aldehyde group to form a Schiff base linkage with the L-cysteine amino group on the surface of the NP, while the other side forms an identical bond with predominantly lysine moieties on BSA.

In this chapter, five new water-soluble, highly luminescent NPs were prepared in a series of one-pot syntheses. Figure 3.1 shows the two ligands used for particle formation. The use of a PEG-based backbone for ligand **1**·($2NH_4^+$) is due to the fact that PEG is known to be a hydrophilic ligand, which allows for the NP to be synthesized and analysed under aqueous conditions, allowing the NP to be studied for its physical (water solubility and stability) and luminescent properties. The second approach will use **2**·($2H^+$) in the NP synthesis as an alternative to (**1**·($2NH_4^+$)), which offers the following advantages: (1) the use of the phosphate-based ligand allows for the use of the same methodologies used for NPs made with **1**·($2NH_4^+$), (2) its short chain length allows for greater ligand surface loading as compared to its PEG counter part, which reduces surface quenching sites (based on lifetime data) and (3), the amine terminus allows for surface functionalization with a variety of different heterobifunctional cross-linking (HBC) ligands using established coupling techniques. All NPs synthesized were doped at 5 atom % of Eu^{3+} or Er^{3+} with respect to the total Ln^{3+} amount, unless otherwise stated.

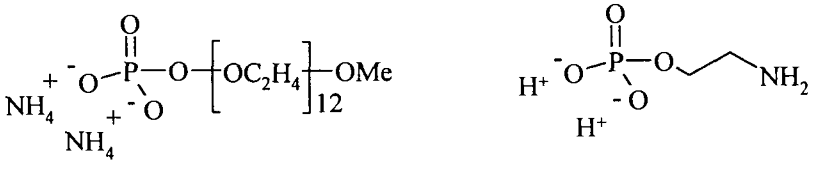

1 ·($2NH_4^+$) **2**·($2H^+$)

*Figure 3.1: Schematic diagram of ligands **1**·($2NH_4^+$) and **2**·($2H^+$).*

3.2 Results and discussion

3.2.1 Results and discussion for Nanoparticles formed with di-Ammonium-[Poly(ethylene glycol)methylether]- Phosphate (1·(2NH$_4^+$))

3.2.1.1 NMR analysis

Synthesis of **1**·(2NH$_4^+$) was done by the reaction of the alcohol-terminated PEG-methyl ether with OPCl$_3$ under an inert environment (N$_{2(g)}$), and isolated by extracting with diethyl ether. The ^{1}H NMR spectrum of **1**·(2NH$_4^+$) after purification shows the double-triplet of the P-(OC**H**$_2$-R) linkage of the PEG unit to the phosphate at 4.0 ppm, which is further supported by ^{13}C NMR with the presence of two doublets at 71.0 ppm P-(O-CH$_2$**C**H$_2$-R) and at 64.3 ppm (P-(O-**C**H$_2$CH$_2$-R), due to phosphorous coupling. The ^{31}P NMR spectrum shows a singlet at 0.9 ppm (O$_3$**P**O-R), which is within the range of phosphate monoesters.

The synthesis of the NP with ligand **1**·(2NH$_4^+$) (referred to simply as **1**·LaF$_3$:Eu) was done by dissolving the ligand and NaF in a solution of water and THF (1:4 ratio v/v), followed by the addition of the Ln^{3+} salts in 2 ml of water. The resulting product was precipitated out of solution, isolated by centrifugation, and purified by triturating in THF. In previous work we have demonstrated that the ligands bind to the NP surface as anions and that the charge compensation is due to excess La^{3+} on the surface.[6] ^{1}H NMR analysis of **1**·LaF$_3$:Eu shows the same peak locations as for the unbound ligand above, but the peaks are heavily broadened due to the inhomogeneous distribution of the magnetic environment around the NP, and a reduction in rotational freedom of the ligand.[6,10] The ^{31}P NMR analysis shows a broad peak (1.3 ppm) due to the monoester phosphate (MOP) product: diester phosphates (DOP) are typically are found about 3-5 ppm upfield from MOP in solution, for which no peak was found in that range.[7] A peak located at about 0.9 ppm is due to inorganic phosphates from the $OPCl_3$ reagent used, for which the presence of these ions in solution does not affect NP formation nor stability. Chemical analysis via elemental analysis or mass spectrum analysis could not be done due to interferences from some unreacted PEG-methylether present in the sample.

3.2.1.2 Particle size analysis

Atomic force microscopy (AFM) of **1**·LaF_3:Eu in Figure 3.2, shows a particle size distribution between 10-30 nm that is centered around 20 nm. The larger features are due to NP agglomeration, which likely occurs during solvent evaporation.

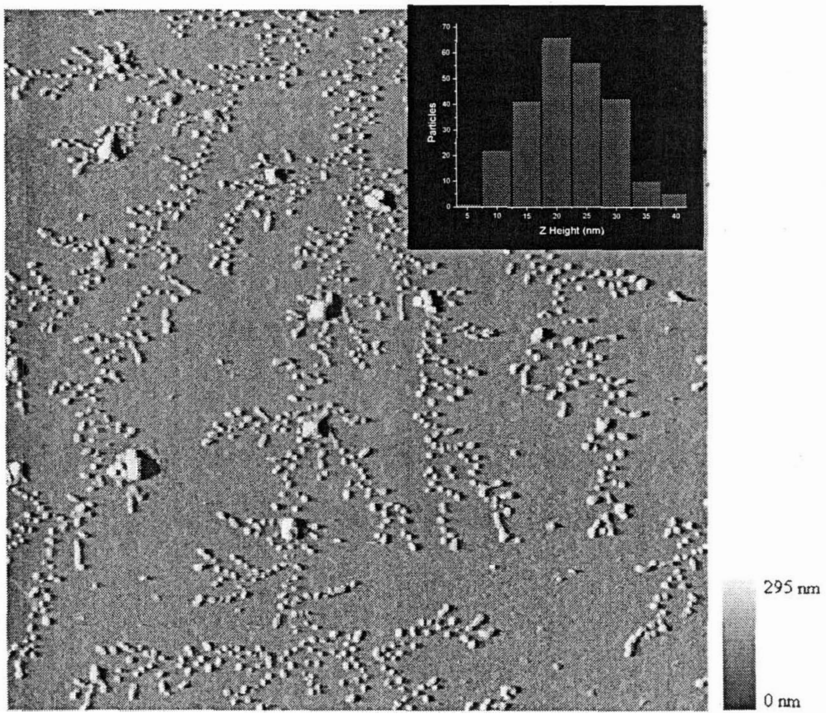

*Figure 3.2: AFM image of **1**·LaF_3:Eu, deposited on a mica substrate from an ethanol suspension.*

3.2.1.3 Spectroscopic analysis

Room temperature fluorescence excitation (λ_{em} = 591 nm) and emission (λ_{ex} = 397 nm) analysis of **1**·LaF_3:Eu, in H_2O, is shown below in Figure 3.3. The excitation spectrum shows the energy levels $^5H_4$ at 318, $^5D_4$ at 361, $^5G_6$ at 376, $^5G_2$ at 380, $^5L_6$ at 397, $^5D_3$ at 414, and $^5D_2$ at 464 nm. The emission spectrum shows the transitions $^5D_1$-$^7F_0$ at 525, $^5D_1$-$^7F_2$ at 554, $^5D_0$-$^7F_0$ at 578, $^5D_0$-$^7F_1$ at 591, $^5D_0$-$^7F_2$ at 613, $^5D_0$-$^7F_3$ at 650, and $^5D_0$-$^7F_4$ at 680-700 nm.

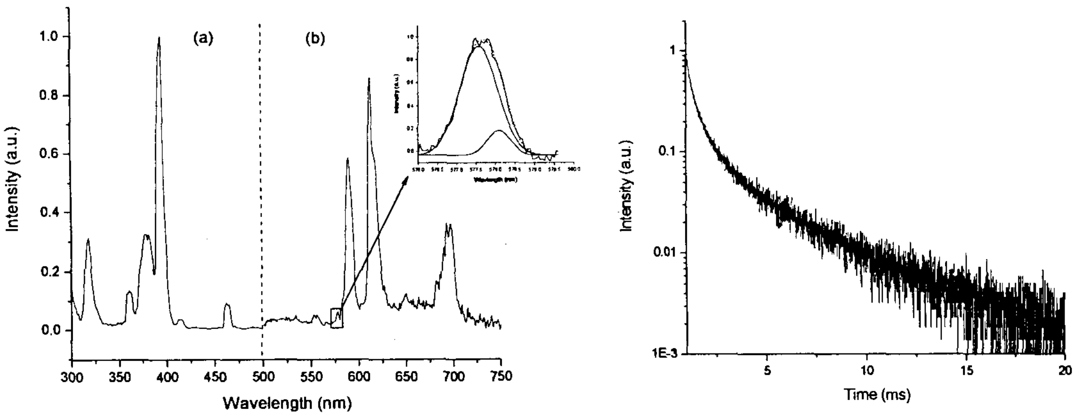

Figure 3.3: Left: (a) excitation and (b) emission spectrum of ***1***·*LaF_3:Eu in H_2O. The inset shows the deconvolution of the high resolution (0.05 nm) 578 nm peak. (λ_{ex} = 397 nm). Right: decay curve of* ***1***·*LaF_3:Eu inH_2O. (λ_{ex} = 464 nm, λ_{em} = 591 nm).*

Qualitative information about the nature and symmetry of the Eu^{3+} ion was determined by analyzing both the shape of the non-degenerate $^5D_0$-$^7F_0$ transition at 578 nm, and the I_{7F2}/I_{7F1} intensity ratio, which in this case was calculated to be 2.0.[8] In comparing the I_{7F2}/I_{7F1} intensity ratio of approximately 1 for bulk LaF_3:Eu NPs, the value of 2.0 for **1**·LaF_3:Eu is due to the fact that within the NP, the Eu^{3+} ions located near the surface of the NP experience a more asymmetric crystal field, which increases the transition probability of the allowed electrical dipole ($^5D_0 \rightarrow ^7F_2$ transition), resulting in an increase in its intensity.[9,10,11] Furthermore, due to the fact that the $^5D_0$ and $^7F_0$ states are both non-degenerate, only a single Gaussian-shaped peak for the transition should appear if all the Eu^{3+} ions are in the same crystal field. The enlarged high resolution insert (0.05 nm) in Figure 3.3, shows two peaks from the deconvolution of the 578 nm emission, indicating that the Eu^{3+} ions are located in more than one crystal field within the NP, which is consistent with the calculated I_{7F2}/I_{7F1} intensity ratio.

The decay curve of the NPs in H_2O, is shown in Figure 3.3. The solution was excited at 464 nm and the emission collected at 591 nm to prevent any lifetime contributions from the $^5D_1$-$^7F_3$ level which overlaps the $^5D_0$-$^7F_2$ transition at 613 nm. The data obtained from the decay curve was fitted with three exponentials; 2.7 ms (37%), 0.6 ms (34%) and 0.2 ms (29%), confirming that there are Eu^{3+} ions located in (at least) two different crystal sites within the NP. The Eu^{3+} ions found within the "bulk" LaF_3 NP (those towards the centre of the core) give rise to the longest lifetimes due to minimal quenching sites, while those located near the surface are more susceptible to non-radiative quenching processes arising from surface-bound water molecules and high energy ligand vibrations, thus reducing the luminescent lifetime.[12]

NPs were also developed for potential biological applications by using the NIR emission lines of Er^{3+} ($^4I_{13/2}$-$^4I_{15/2}$ transition at 1530 nm), arising from the fact that for deeper signal depth penetration of tissue samples, NIR emission reduces the effects of absorption from water, tissue and blood (hemoglobin in particular), and scatter from differences in skin tissue density, as compared to the use of visible light.[13,14]

Figure 3.4 shows the emission spectrum (λ_{ex} = 488 nm) and decay curve of **1**·LaF$_3$:Er in D$_2$O (weaker signal intensity is encountered when measured in H$_2$O), which the emission spectrum shows the expected transition at 1530 nm ($^4I_{13/2}$-$^4I_{15/2}$), while the analysis of the decay curve for the NP was fitted suitably with 3 exponentials: 50 μs (45%), 11 μs (37%), and 2 μs (22%). Despite the fact that Er^{3+} ions can have very long lived lifetimes, it is clear that there is still significant quenching in relation to the theoretical lifetime of up to 20 ms.[15] The effects of surface-related quenching effects can be reduced by the formation of core-shell NPs, where the growth of a layer of LaF$_3$ around the core minimizes contact between the dopant ions and sources of non-radiative quenching processes.[10] Refer to Table 3.1 for full luminescence lifetimes.

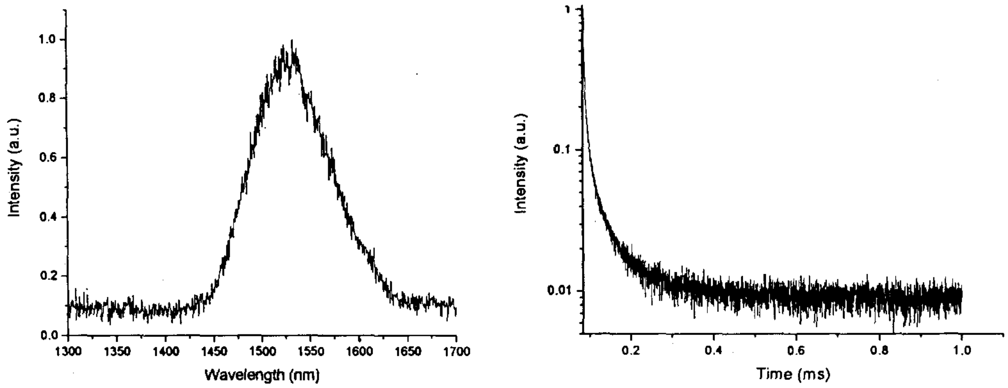

Figure 3.4: Left: emission spectrum of 1·LaF$_3$:Er in D$_2$O. (λ_{ex} =488 nm). Right: decay curve of 1·LaF$_3$:Er in D$_2$O. (λ_{ex} = 488 nm, λ_{em} = 1530 nm).

3.2.2 Nanoparticles formed with 2-Aminoethyl Dihydrogen Phosphate (2·(2H$^+$)).

3.2.2.1 NMR analysis

Synthesis of **2**·LaF$_3$:Eu was done in order to study the spectroscopic effects of amine-terminated ligands on the NP for subsequent use (HBCs). Synthesis of the NPs was done by dissolving **2**·($2H^+$) in water at 37 °C, neutralizing with NH_4OH_{aq}, followed by the addition of NaF and Ln^{3+} salts (dissolved in water). The NPs were precipitated with acetone and isolated by centrifuge, and triturated in acetone.

Characterization of the NP was done by NMR (^1H, ^{13}C, ^{31}P) and fluorescence analysis. The ^1H NMR spectrum of **2**·LaF_3:Eu shows the two CH_2 peaks located at 4.0 ppm and 3.2 ppm, and the ^{13}C NMR spectrum shows peaks at 40.5 ppm (-$OCH_2CH_2NH_3^+$) and 60.8 ppm (-$OCH_2CH_2NH_3^+$), all broadened as expected. The ^{31}P NMR spectrum in Figure 3.5 shows a broad peak (1.3 ppm) overlapping a very broad peak (4.0 to -6.0 ppm), arising from different coordination dynamics of the ligands on the surface of the NP. That is, the broad peak at 1.3 ppm is due to restricted mobility of the ligand on the NP, and the very broad peak arises from even more restricted mobility at a different location on the NP. The difference in restricted mobility could be due to the phosphate units being coordinated to the crystal facet or crystal edge of the NP. This is consistent with the line broadening effects seen with core-shell NPs in other work from us, where a shell of LaF_3 is grown around the LaF_3:Eu core, in which the effect of paramagnetic Eu^{3+} is not the cause.[10]

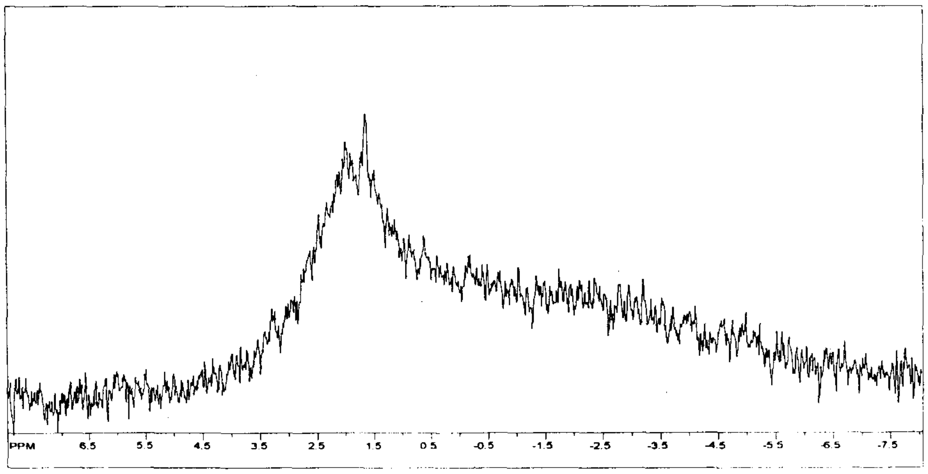

*Figure 3.5: ^{31}P NMR of **2**·LaF_3:Eu in D_2O*

3.2.2.2 Particle size analysis

AFM analysis of **2**·LaF_3:Eu was carried out by depositing the NPs on a mica surface from an ethanol suspension, with a particle size distribution from 5-50 nm which centered at 10 nm, in accordance to what was expected (see Figure 3.6). In comparison to the **1**·LaF_3:Eu, the size of **2**·LaF_3:Eu is anticipated to be within the range of about 5-15 nm due the fact that **2**·($2H^+$) is significantly shorter in length than **1**·($2NH_4^+$), and due to the fact that XRD analysis shows that the core of the NP is on average between 3-6 nm in diameter, which is in agreement with TEM analysis of similar LaF_3:Eu-based NPs.[9] Furthermore, dynamic light scattering (DLS) experiments in H_2O yields an effective diameter of 12 nm, with a size distribution that tails off at about 40 nm, which is in agreement with AFM measurements.

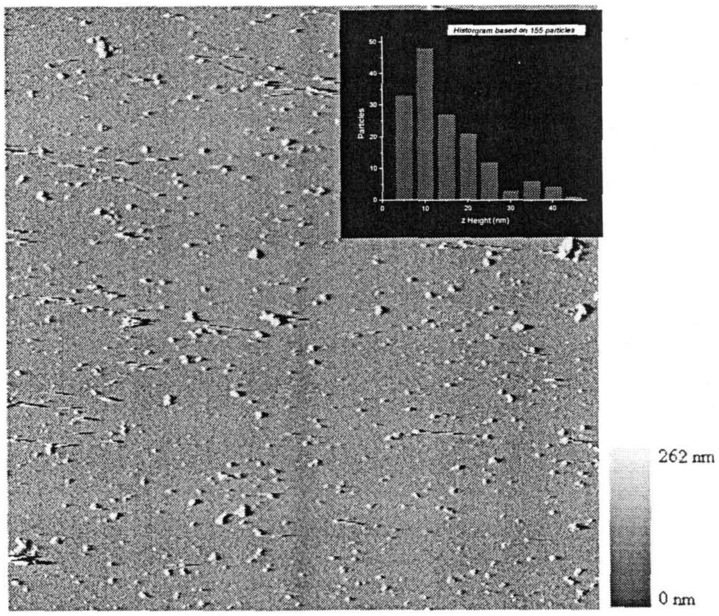

Figure 3.6: AFM image of 2·LaF_3:Eu deposited on a mica substrate from an ethanol suspension.

As for the size histogram, the procedure used for NP synthesis is not optimized to produce a narrow size distribution, as such, a wide size distribution does occur in which severe particle agglomeration typically yields NPs in excess of 50 nm.

3.2.2.3 Spectroscopic analysis

Figure 3.7 shows the emission spectrum and decay curve (in H_2O) of **2**·LaF_3:Eu. As can be seen, the expected Eu^{3+} peaks are present, in which the enlarged area at 578 nm can be fitted with two Gaussian peaks overlapping each other, arising from Eu^{3+} ions present in both the bulk and near or on the surface of the NP (vide supra). As observed before, the 612 nm peak dominates the emission spectrum (I_{7F2}/I_{7F1} ratio of 1.5) indicating that the Eu^{3+} ions located near the surface of the NP are in a more asymmetric crystal field, similar to **1**·LaF_3:Eu. The decay curve was fitted with 3 exponentials with lifetime values of 5.8 ms (50%), 2.5 ms (39%) and 0.9 ms (11%), which is consistent with Eu^{3+} ions being located in different crystals sites within the NP.[6,9,11]

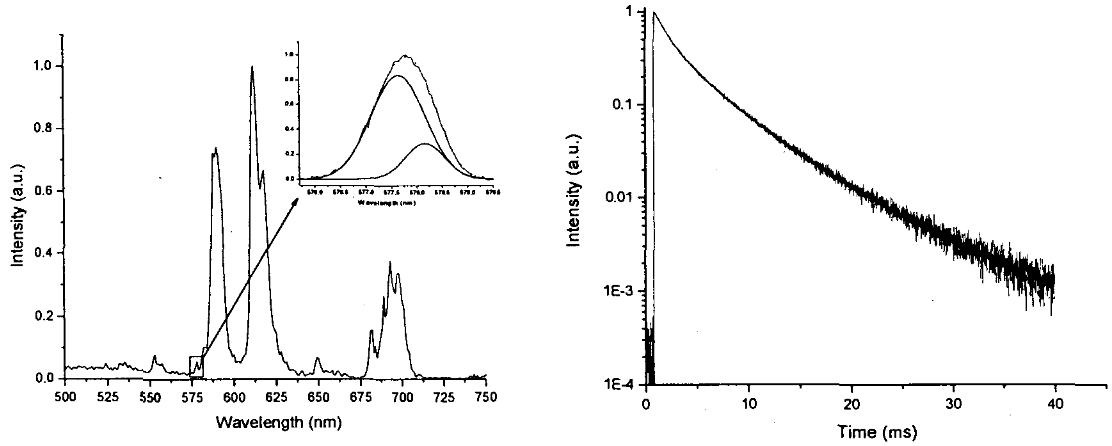

Figure 3.7: Left: (a) excitation and (b) emission spectrum of **2**·LaF_3*:Eu in* H_2O*. The inset shows the deconvolution of the high resolution (0.05 nm) 578 nm peak.* (λ_{ex} *= 397 nm). Right: decay curve of* **1**·LaF_3*:Eu in*H_2O*.* (λ_{ex} *= 464 nm,* λ_{em} *= 591 nm).*

In relation to **2**·LaF_3:Eu, the shorter lifetimes measured for **1**·LaF_3:Eu are likely a result of reduced ligand loading on the surface of the NP due to the bulkiness of the PEG unit as compared to the 2-aminoethyl unit of **2**·($2H^+$), therefore increasing the number of possible quenching sites on the surface of the NP.[11] This effect is expected to be amplified with the H_2O:THF (1:4 v/v) solvent mixture used in the synthesis of **1**·LaF_3:Eu, which increases effective size in a lateral sense due to the ligands coiling, both by individually and collectively. Furthermore, even thought the decay curve for **2**·LaF_3:Eu was fitted with 3 lifetimes, and spectral deconvolution of the 578 nm peak showed only two gaussian curves, the seeming contradiction of the two methods results from the fact that contribution from the $^5D_1$-$^7F_3$ transition at 580 nm does influence the shape of the 578 nm transition due to overlapping peaks,[16] thus spectral deconvolution can only be treated qualitatively.

To test the near-infrared (NIR) luminescent capabilities of the particles, the synthesis of **2**·LaF_3:Er was carried out in which the emission spectrum, in D_2O, shows the same $^4I_{13/2}$-$^4I_{15/2}$ transition at 1530 nm seen for **1**·LaF_3:Er (Figure 3.4). The decay curve was fitted with 2 exponentials yielding lifetime values of 118 μs (82%) and 17 μs (17%), which is within range of **1**·LaF_3:Er, indicating that the Er^{3+} ions are still significantly quenched by solvent and ligand interactions. Improvement of the luminescent lifetimes can be achieved by forming core-shell NPs, thus reducing solvent quenching effects (vide supra).

3.2.2.4 Quantum yield analysis

Due to the low absorption coefficients of most Ln^{3+} ions, estimation of quantum yields is not easily feasible and therefore use of NPs with a $La_{0.4}F_3$:$Ce_{0.45}$,$Tb_{0.15}$ (LaF_3:Ce,Tb) matrix was carried out. The Ce^{3+} ion has a relatively broad absorption band from 200-300 nm due to allowed 4f-5d transition, and it is known that Ce^{3+} undergoes energy transfer to other Ln^{3+} ions, in particular with Tb^{3+} which emits in visible region (green).[11] Quinine sulfate was chosen as the reference dye for several reasons: (1) its emission band overlaps those of the Tb^{3+} ion, (2) the excitation band of quinine sulfate has a large Stoke's shift, minimizing re-absorption of emission light, and finally (3), the quantum yield of quinine sulfate in an aqueous solution (1M H_2SO_4) is $\Phi = 55\%$.[17] The NPs were calculated to have a Φ value of 20% ± 2% in H_2O, which is in accordance to a reported value of 19% using the same NP matrix, but stabilized with a different ligand in dichloromethane.[6,9,11] Increases in the quantum yield to 38% was achieved upon the addition of D_2O, as a result of exchanging surface bound water molecules with deuterium, in which the lower vibration OD bonds quench less efficiently than the high energy OH bonds.[11]

3.3 Conclusions

A one-step synthesis of optically robust, water-soluble Ln^{3+}-doped LaF_3 nanoparticles (NPs) was achieved through the use of the $(RO)PO_3^{2-}$ coordinating unit with PEG-based and amine-terminated ligands. The synthesis demonstrated that the NPs can be doped with Eu^{3+} and Er^{3+} ions, which exhibited luminescence in the visible (300-750 nm) and NIR (750-2400 nm) region, under aqueous conditions. Analysis of the emission spectra showed that the Eu^{3+} ions are located in more than one crystal field due to the asymmetry of the 578 nm emission, which was further supported by the multi-exponential decay of the Eu^{3+} doped NPs, which is in full agreement with earlier work. Analysis of the I_{7F2}/I_{7F1} intensity ratio, which was greater than 1 for both NPs, indicated that the Eu^{3+} ions that were located near the surface of the NP experienced a more asymmetric crystal field due to the coordination of an oxygen atom from the ligands. The lifetime values calculated were in the millisecond range for Eu^{3+} doped NPs, and in the 50-100 microsecond range for Er^{3+} doped NPs. The robustness of the method to form NPs with two different functionalized ligands was confirmed by particle size analysis, which showed that the particles remained within the nanometer range.

3.4 Table

Compound	**Solvent**	τ_1	τ_2	τ_3
1·LaF_3:Eu	H_2O	2.7 ms (37%)	0.6 ms (34%)	0.2 ms (29%)
1·LaF_3:Er	D_2O	50 μs (45%)	11 μs (37%)	2 μs (22%)
2·LaF_3:Eu	H_2O	5.9 ms (50%)	2.5 ms (39%)	0.9 ms (11%)
2·LaF_3:Er	D_2O	118 μs (82%)	17 μs (17%)	------------

Error on the measured τ values is ± 5% for duplicates.

Table 3.1: Luminescent lifetimes (and percent contribution)

3.5 Experimental

3.5.1 *Experimental conditions*

All chemicals were obtained from Aldrich and used without further purification unless otherwise indicated. The source of water used consisted of distilled water. All nanoparticles (NPs) were made with LaF_3 at 5% Eu^{+3} or Er^{3+} atom doping on the total Ln^{3+} amount. NPs used for quantum yields calculations were made with an LaF_3:Ce,Tb matrix, with La^{3+} at 40%, Ce^{3+} at 45%, and Tb^{3+} at 15% atom doping on the total Ln^{3+} amount.[11] The reference material for quantum yield calculations was quinine sulfate in a 1M H_2SO_4 solution, with $\Phi_{ref} = 55\%$.[17] The equation[9] used to calculate the quantum yield is defined below where *n* is refractive index, *I* is the measured intensity, and *A* is the absorbance of the solution, and Φ_{ref} is the quantum yield of the reference material. The error was estimated at 2% for duplicate measurements.

$$\Phi = \left[\frac{n^2_{sample} I_{sample} A_{ref}}{n^2_{ref} I_{ref} A_{sample}}\right] \Phi_{ref}$$

All steady-state fluorescence analyses were done using an Edinburgh Instruments FLS 920 fluorescence system, which was equipped a CW 450W xenon arc lamp via a M300 single grating monochromator. A red-sensitive peltier-cooled Hamamatsu R955 photomultiplier tube (PMT), with a photon-counting interface, was used for analyses between 200-850 nm, and a N_2-cooled (-80 ^{0}C) Hamamatsu R5509 PMT was used for analyses between 400-1700 nm. All emission and excitation analyses in the visible region were measured with a 1 nm resolution, or 0.05 nm for high resolution analyses, and NIR emission analyses were done with a 5 nm resolution. Lifetime analyses were done by exciting the solutions with a 10 Hz Q-Switched Quantel Brilliant, pumped by a Nd:YAG laser, with an optical range from 410-2400 nm, and collecting the emission using the respective detectors mentioned above. Decay curves were measured with a 0.2 ms and a 0.01 ms lamp trigger delay for the R955 and R5509 PMT, respectively.

All lifetime analyses were calculated using the Edinburgh Instruments F900 software and signal intensities greater than 1 % of the maximum intensity were included, and were fitted so as to obtain χ^2 values from 1.0 to 1.3. If two exponentials did not give an acceptable fit, three exponentials were taken. Reported lifetime and percent contribution are only treated in a qualitative sense, and errors were estimated to be 5% based on duplicate measurements. Peak deconvolution was done using software from Originlab (Origin 7.5).

All ^{1}H and ^{13}C NMR analysis was done using a Bruker 300 MHz NMR instrument, and ^{31}P NMR was done on a Bruker AMX 350 MHz instrument. Chemical shifts of ^{31}P NMR were measured relative to an external standard of 85% H_3PO_4. No NMR analysis was carried out on Er^{3+}- and Tb^{3+}-based NPs due to severe line broadening.

Atomic force microscopy (AFM) was done using a Thermomicroscope Explorer. Samples were deposited from an ethanol suspension on a freshly cleaved mica substrate, and the ethanol allowed to fully dry. Dynamic light scattering (DLS) experiments were carried out on a Brookhaven Instruments photon correlation spectrometer equipped with a BI-200SM goniometer, a BI-9000AT digital autocorrelator, and a Melles Griot He-Ne Laser (632.8 nm) with maximum power output of 75 mW. All water and NP solutions were filtered through 0.45 μm Teflon syringe filters. Sample vials used for measurements were rinsed 3 times with the above filtered water. Final sample concentration used was 0.5 mg·ml^{-1}. DLS experiments were done at a 90° angle.

3.5.2 Synthesis

di-ammonium-[poly(ethylene glycol)methylether]phosphate (1·(2NH$_4^+$): A solution of 10.5 g (18.5 mmol) poly(ethylene glycol) methyl ether (ca. Mw ~ 550) with molecular sieves was stirred overnight to remove residual water. Then 20 ml of distilled THF (from Na$^+$/benzophenone) was added, and slowly dropped to $OPCl_3$ (1.42 g, 9.2 mmol) at –15 °C under Ar. The solution was slowly allowed to warm to room temperature and stirred for two hours, followed by the addition of 1 ml of water and vigorously stirred for 1 hour. Subsequently, 100 ml of ethyl acetate was added and the organic layer was extracted, dried over $MgSO_4$, and evaporated to dryness. Finally, 20 ml of hexane was added and NH_3 was bubbled through the solution. The solvent was removed by rotary evaporation, and then dried under reduced pressure. The product was triturated in methanol and THF, and isolated by centrifuge. A white semi-solid remained. Impurities due to unreacted PEG are present at less than 5%, and the inorganic phosphate is a result of phosphate hydrolysis. ^{1}H NMR: δ (D_2O) 3.9 (dt, $^3J_{HP}$ = 8.1 Hz, $^3J_{vic}$ = 6.4 Hz, 2H, P-(OCH_2-)), 3.8 - 3.4 (m, 49H, (-CH_2OCH_2-)$_n$ of the PEG), 3.4 (s, 3H, -OCH_3); ^{13}C NMR: δ (D_2O) 71.0 (d, $^3J_{CP}$ = 7.9 Hz, P-(O-CH_2CH_2-O-R)$_2$), 69.8 (m, (CH_2-O-CH_2)$_n$), 64.3 (d, $^2J_{CP}$ = 5.5 Hz, (P-(O-CH_2CH_2-R)$_2$), 58.7 (s, R-O-CH_3); ^{31}P NMR: δ (D_2O) 0.9 (s, O_3PO-R).

1·LaF$_3$:Eu: At room temperature, a solution of **1**·(2NH$_4^+$) (1.15 g, 0.95 mmol) was dissolved in 30 ml of THF and stirred for 15 minutes, followed by the addition of NaF (0.13 g, 3.00 mmol) in 7 ml of H_2O. The solution was stirred for 15 minutes followed by the drop-wise addition of $La(NO_3)_3{\cdot}6H_2O$ (0.54 g, 1.26 mmol) and $Eu(NO_3)_3{\cdot}5H_20$ (0.03 g, 0.04 mmol) in 2 ml of H_2O. The suspension was stirred for 1 hour, and then the solvent was removed by rotary-evaporation, and then dried under reduced pressure overnight. The product was then triturated with 20 ml of THF (a loose white suspension formed), separated by centrifuge, and then washed and separated with THF three times. The final product was a white, highly water-soluble powder. Some hydrolyzed phosphates, as inorganic phosphate and polyphosphates, were present but did not impede NP formation. ^{1}H NMR: δ (D_2O) 4.0 (bs, 2H, $PO\mathbf{CH_2}$-), 3.2 (bs, 54H, -$\mathbf{CH_2}$-O-$\mathbf{CH_2}$-), 3.4 (s, 3H, -$\mathbf{CH_3}$); ^{31}P NMR: δ 1.3 (s, $O_3\mathbf{P}O$-R).

1·LaF$_3$:Er: The same method was used as above, but with $Er(NO_3)_3{\cdot}5H_2O$ (0.03 g, 0.27 mmol).

2·LaF$_3$:Eu: A solution of **2**·(2H$^+$) (0.14 g, 1.02 mmol) in 25 ml of water was neutralized with $NH_4OH_{(aq)}$, followed by the addition of NaF (0.13 g, 3.00 mmol). The solution was heated to 37 °C, then followed by the addition of $La(NO_3)_3{\cdot}6H_2O$ (0.54 g, 1.26 mmol) and $Eu(NO_3)_3{\cdot}$ $5H_2O$ (0.03 g, 0.04 mmol) in 2 ml of water. The solution was added drop-wise and stirred at 37 °C for 16 hrs, yielding a clear solution. Isolation of the particles was done by removing the water until the product was reduced to a paste-like consistency, then redissolved with 5 ml of water and precipitated with acetone. The particles were then isolated by centrifuge, and the supernatant poured off, and the remaining precipitate was then triturated with acetone, separated by centrifuge, and dried under reduced pressure. ^{1}H NMR: δ (D_2O) 4.0 (bs, 2H, $PO\mathbf{CH_2}CH_2NH_3^+$), 3.2 (bs, 2H, $POCH_2\mathbf{CH_2}NH_3^+$); ^{13}C NMR: δ ($D_2O$) 61.0 (bs, $PO\mathbf{C}H_2CH_2NH_3^+$), 40.0 (bs, $POCH_2\mathbf{C}H_2NH_3^+$); ^{31}P NMR: δ ($D_2O$) 1.3 (bs, $O_3\mathbf{P}O$-R) and -1.5 (very bs, $O_3\mathbf{P}O$-R). For comparison, the NMR data for

2·($2H^+$) are given here as well; ^1H NMR: δ (D_2O) 4.1 (dt, $^3J_{HP}$ = 7.1 Hz, $^3J_{vic}$ = 5.7 Hz, 2H, $POC\mathbf{H_2}CH_2NH_3^+$), 3.2 (t, $^3J_{vic}$ = 5.7 Hz, 2H, $POCH_2C\mathbf{H_2}NH_3^+$); ^{13}C NMR: δ (D_2O) 61.1 (d, $^2J_{CP}$ = 5.0 Hz, $POCH_2CH_2NH_3^+$), 40.2 (d, $^3J_{CP}$ = 8.2 Hz, $POCH_2\mathbf{C}H_2NH_3^+$); ^{31}P NMR: δ (D_2O) 0.4 (s, $O_3\mathbf{P}O$-R).

2·LaF_3:Er: same method as above, but with $Er(NO_3)_3 \cdot 5H_2O$ (0.03 g, 0.27 mmol).

2·LaF_3:Ce,Tb: Same procedure **2**·LaF_3:Eu, but with $Ce(NO_3)_3 \cdot 5H_2O$ (0.58 g, 1.31 mmol), $Tb(NO_3)_3 \cdot 6H_2O$ (0.21 g, 0.55 mmol) and $La(NO_3)_3 \cdot 6H_2O$ (0.55 g, 1.26 mmol).

3.6 References

[1] M.J Roberts, M.D. Bentley, J.M. Harris (2002) *Adv. Drug Deliv. Rev.* **54**, 459-476.

[2] H. Otsuka, Y. Nagasaki, K. Kataoka (2003) *Adv. Drug Deliv. Rev.* 55, 403-419.

[3] M. Zheng, Z. Li, X. Huang (2004) *Langmuir* **20**, 4226-4235.

[4] K.Aslan, C.C. Luhrs, V.H. Perez-Luna (2004) *J. Phys. Chem. B* **108**, 15631-15639.

[5] N.M. Mamedova, N.A. Kotov, A.L. Rogach, J. Studer (2001) *Nano Lett.* **6**, 281-286.

[6] J. W. Stouwdam, F. C. J. M. van Veggel (2004) *Langmuir* 20, 11763-11771.

[7] B.L. Turner, N. Mahieu, L.M. Condron (2003) *Soil Sci. Soc. Am. J.* **67**, 497-510.

[8] M. H. V. Werts, R.T.F. Jukes, J. W. Verhoeven (2002) *Phys. Chem. Chem. Phys.* **4**, 1542-1548.

[9] J. W. Stouwdam, F. C. J. M. van Veggel (2002) *Nano Lett.* 7, 733-737.

[10] V. Sudarsan , F.C.J.M. van Veggel , R.A. Herring, M. Raudsepp (2005) *J. Mater. Chem.* **15**, DOI: 10.1039/b413436b.

[11] J. W. Stouwdam, G.A. Hebbink, J. Huskens, F.C.J.M. van Veggel (2003) *Chem. Mater.* **15**, 4604-4616.

[12] K. Driesen, R van Deun, C. Görller-Walrand, K. Binnemans (2004) *Chem. Mater.* **16**, 1531-1535.

[13] D. R Larson, W.R. Zipfel, R.M. Williams, S.W. Clark, M.P. Bruchez, F.W. Wise, W. W. Webb (2003) *Science* **300**, 1434-1436.

[14] Y. T. Lim, S. Kim, A. Nakayama, N.E. Stott, M.G. Bawendi, J.V. Frangioni (2003) *Mol. Imaging* **1**, 50-64.

[15] M. J. De Dood, L. H. Slooff, A. Polman, A. Moroz, A. van Blaaderen (2001) *Appl. Phys. Lett.* **22**, 3585-3587.

[16] N. Arnaud, J. Georges (2003) *Spectrochim. Acta Part A* **59**, 1829-1840.

[17] D.F. Eaton (1988) *Pure Appl. Chem.* **60**, 1107-1114.

Chapter 4

Surface Modification and Biotin-Avidin Binding Studies[1]

4.1 Introduction

It is well known that many proteins exhibit fluorescent properties when functionalized with phenylalanine or tryptophan, however the fluorescence is too weak and non-specific for detections at low protein concentration. As such, surface modification of the protein is carried out by taking advantage of two to three functional groups (amino, thiol, or carboxyl groups) on the protein in order to derivatize it with a strongly fluorescent probe.[1] Typically bioconjugation reactions are first carried out by modifying the surface of the probe with a heterobifunctional cross-linker (HBC), which subsequently defines the biological activity of the probe based on the functional group available at the termini of the HBC, (often consisting of a biotin[2], *N*-hydroxy-succinimide[3] (NHS), or a maleimide[4] moiety).

Of the routes taken, probe-functionalization with biotin is frequently used as a proof-of-principle for bioconjugation due to the fact that the biotin-avidin system is a well studied "lock and key" system, with an affinity constant in the range of 10^{15} M^{-1}, which is one of the highest known in nature between a protein and a ligand.[5] Typically two different methods are employed for biotin-avidin binding experiments: particle support or solid phase support (SPS). In either case, there are several important considerations:

---

[1] The major part of the work in this chapter was accepted for publication: P.R. Diamente, F.C.J.M. van Veggel (2005) *J. Fluor.*.

surface area available, reactivity and stability of bound reagents, and ease of coupling. Surface area has a major effect on the sensitivity and kinetics of enzyme immunoassay (EIA).

Microplates, a form of SPS, have limited surface area which results in slow reactions. Membranes provide higher surface area and capacity by permitting reactions to occur throughout the thickness of the support. Finally, microparticles (MP) can provide orders of magnitude more surface area, depending on the particle size selected.[6]

In this chapter, control experiments using *N*-acryloxysuccinimde (**3**) (Figure 4.1) will be carried out in order to asses the feasibility of using amine-terminated NPs, **2**·LaF_3:Ln, to under go surface modifications by two different methods: ligand modification and NP surface modification. The methodologies established in the first part of the chapter will then be utilized towards the incorporation of two HBCs, **5** and **6** (Figure 4.3), which are both functionalized with NHS and biotin at opposite termini.

To evaluate the biotin-binding capabilities of the functionalized NPs, the use of MP-bound avidin was chosen. Due to the high surface area available for reaction and its insolubility in solution, the simple purification and isolation techniques of the reacted MPs allows them to be transferred to regular fluorescent-grade cuvettes for luminescent analysis.

4.2 Results and discussion

4.2.1 Control experiments

To establish the viability and stability of the method for surface modification of the NPs with an amine-reactive HBC ligand (**5** and **6**), control experiments were done on

2·LaF$_3$:Eu using *N*-acryloxysuccinimide (**3**) (Figure 4.1). Ligand **3** was used as a model HBC ligand for control experiments due to its activated ester, which reacts specifically with primary and secondary amines, and its vinyl group, yielding an acrylamide-terminated ligand. The advantage of the vinyl group is that it offers the ability to monitor the reaction by NMR without overlap of any other peaks, in addition to its linear structure minimizes steric hindrance during NP formation. As a result, the reaction of **3** with **2**·(2H$^+$) could be carried out by one of two different methods, NP synthesis (**A**) and surface reaction (**B**), with **2**·LaF$_3$:Ln^{3+} as a comparison for their physical and spectroscopic properties

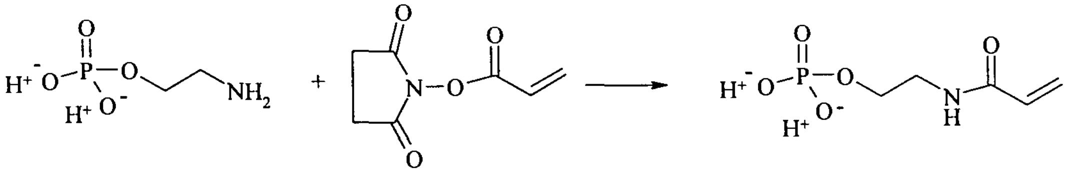

2·(2H$^+$) **3** **4**·(2H$^+$)

*Figure 4.1: Schematic diagram of ligand **2**·(2H$^+$) reacting with 3 to yield **4**·(2H$^+$).*

4.2.1.1 NMR analysis

Functionalization of the NP by method **A** (NP synthesis) first involves reacting **2**·(2H$^+$) with **3**, in a defined molar ratio (a 1:0.2 molar ratio was used, respectively), forming a ligand mixture of **2**·(2H$^+$) and 2-(acrylamide)ethyl phosphate (**4**·(2H$^+$)) in a 1:0.2 molar ratio, which was then used directly in the NP synthesis, based on methods in Chapter 3. The side product *N*-hydroxysuccinimide (NHS) formed during the reaction of **2**·(2H$^+$) with **3** was easily washed away during purification (as monitored by ^{1}H NMR).

The ^{1}H NMR gave the expected broad peaks seen for **2**·**4**·LaF$_3$:Eu, in addition to the broad vinyl acrylamide peaks at 6.2 ppm and 5.8 ppm. The ^{31}P NMR analysis showed a broad peak at 1.3 ppm overlapping an even broader peak from 4.0 to -6.0 ppm, as seen with **2**·LaF$_3$:Eu (refer to Figure 3.5 in Chapter 3). Removal of **2** and **4** to estimate the molar ratio of the ligands on the surface of the NP was accomplished by adding 0.3 ml of citrate buffer solution (buffer pH ~ 6) to the NMR tube, and letting it sit for 2 days. The resulting ^{1}H NMR ratio of the ligand mixture **2**·(2H$^+$) and **4**·(2H$^+$) was calculated to be approximately 20%, which is in accordance to what was expected due to the fact that both ligands are linear structures in solution, resulting in minimal steric hindrance of the two ligands after surface coordination.

The second method developed, method **B** (surface reaction), utilized **2**·LaF$_3$:Ln (Chapter 3) that were reacted directly with a small amount of **3** in solution. The ^{1}H NMR of the NPs show the same peak positions and line broadening as those from method **A**, indicating that the surface reaction was successful. Calculation of the amount of **3** reacted on the surface was not carried, out but is expected to be in excess of 50%; a pre-defined molar ratio beyond 1:0.5 resulted in a significant decrease in NP solubility due to the vinyl-terminated ligands. Some control over the surface concentration of acrylamide can be achieved by varying the amount of **3** used in the reaction.

4.2.1.2 Spectroscopic analysis

Analysis of the emission spectra in Figure 4.2 of the NPs from method **A** & **B** show the same I_{7F2}/I_{7F1} intensity ratio of 1.6, with the enlarged area at 578 nm showing near identical, asymmetrical peaks. The decay curves for the both methods were fitted with 3 exponentials, which were within experimental error (± 5% in duplicate) of the unreacted **2**·LaF$_3$:Eu, further demonstrating that the ligand mixture of **2**·(2H$^+$) and **4**·(2H$^+$) does not alter the NP synthesis. Synthesis of the NPs doped with Er^{3+} by method **A** shows the expected Er^{3+} transition ($^4I_{13/2}$-$^4I_{15/2}$) at 1530 nm, as seen for **1**·LaF$_3$:Er (Figure 3.4 in Chapter 3), with a decay curve that was fitted with 3 exponentials, yielding lifetime values of 50 μs (32%), 12 μs (43%), and 3 μs (25%).

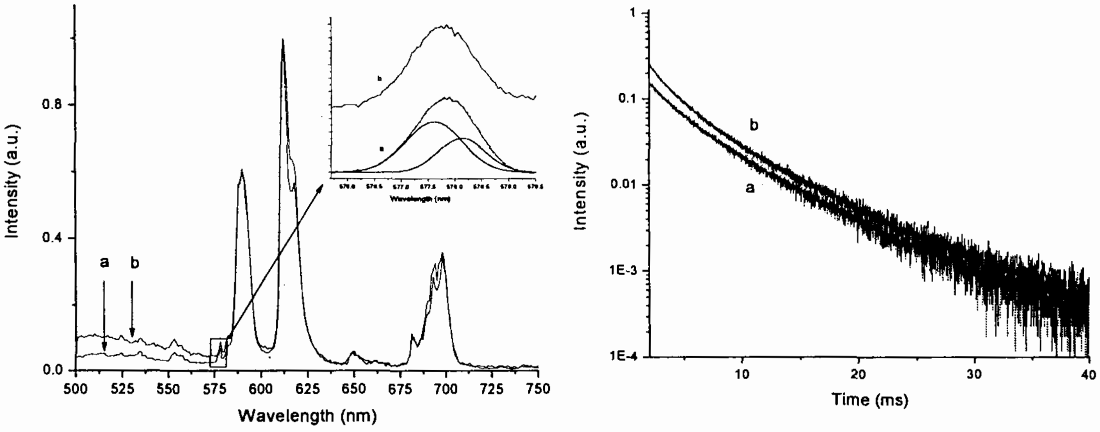

*Figure 4.2: Left: emission spectra of surface reacted **2**·LaF$_3$:Eu with **3** (line a), and **2**:**4**·LaF$_3$:Eu (line b). The spectra are offset for clarity. The inset shows the deconvolution of the high resolution (0.05 nm) 578 nm peak. (λ_{ex} = 397 nm). Right: decay curves of surface reacted **2**·LaF$_3$:Eu with **3** (line a), and **2**:**4**·LaF$_3$:Eu (line b). The curves are offset for clarity. (λ_{ex}= 464 nm, λ_{em} = 591 nm).*

4.2.2 Use of biotin-based HBCs

Having demonstrated that the spectroscopic properties were not altered when the NPs were synthesized by method **A** or **B**, the methodologies established above were used with two new HBC; biotin-*N*-hydroxysuccinimide (**5**) and biotin-PEG$_4$-*N*-

hydroxysuccinimide (**6**), as shown in Figure 4.3. Both ligands are reacted with **2**·(2H$^+$) at a pre-defined molar ratio, through the use of the activated ester present on each HBC, in order to have both **2**·(2H$^+$) and **7**·(2H$^+$) (or **8**·(2H$^+$)) on the NP surface. In particular, ligand **8**·(2H$^+$) has the added advantage of having a 4 unit PEG spacer in order to increase water solubility of the ligand/NP, and helps to reduce non-specific binding of the NP to a biological-based surface (refer to Chapter 2 and 3).

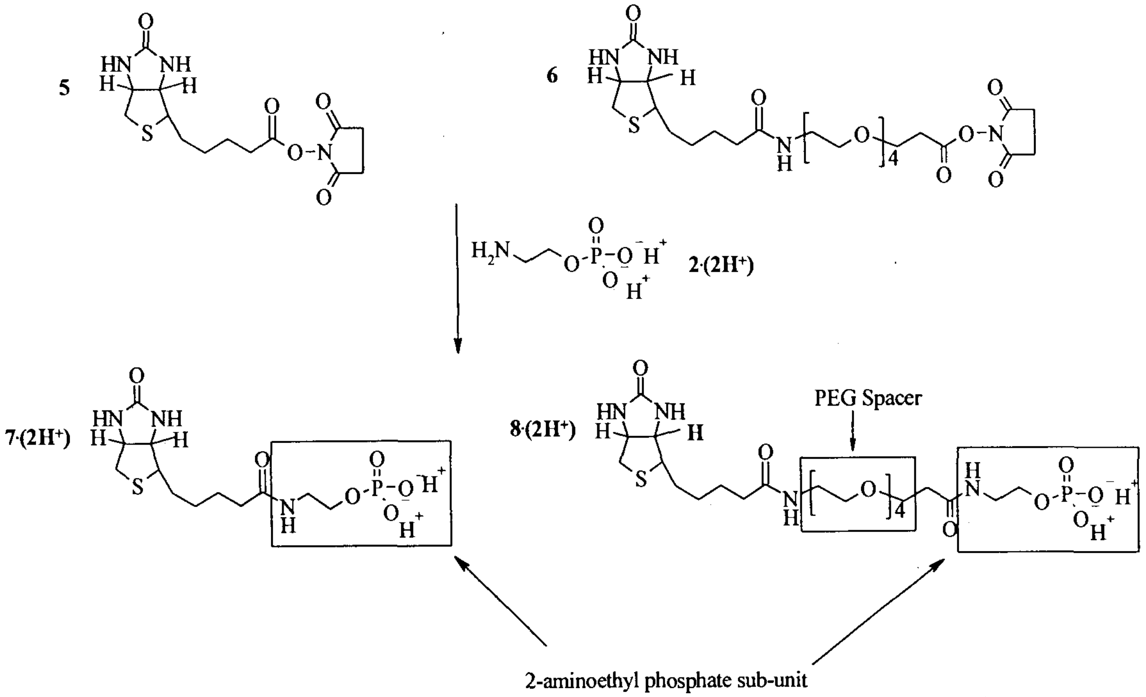

Figure 4.3: Schematic diagram of the synthesis of ligands 7·(2H$^+$) and 8·(2H$^+$).

4.2.2.1 NMR analysis

Synthesis of the NPs followed the same procedures as **2**:**4**·LaF_3:Ln^{3+}, where two different methods were used (vide supra), where ligands **5** and **6** were used in substitute of **3**. Briefly, synthesis of the NPs by method **A** was done by dissolving **2**·(2H$^+$) in water at 37 °C, neutralizing with $NaOH_{(aq)}$, followed by the addition of **5** or **6** (dissolved in a minimum of DMSO) at the desired molar ratio. The reaction was carried out for 1 hr under constant stirring, followed by the addition of NaF and the Ln^{3+} salts. The NPs were precipitated with acetone, isolated by centrifuge and washed with acetone to remove most of the residual NHS and DMSO.

The ^1H NMR in Figure 4.4 shows the expected peaks of the ligand mixture **2**·($2H^+$):**7**·($2H^+$), at 3.9 ppm ($POC\mathbf{H_2}CH_2NH_2$) and 3.8 ppm ($POC\mathbf{H_2}CH_2NHR$) respectively, correspond to a ligand mixture with a molar ratio of 1:0.1, respectively, which was further supported by ^{13}C NMR. The ^{31}P NMR shows two broad peaks of **2**·($2H^+$) (3.7 ppm) and **8**·($2H^+$) (2.8 ppm), with an integration of 1 and 0.1 corresponding to the presence of both ligands in their expected molar ratios (refer to experimental section for full NMR assignments).

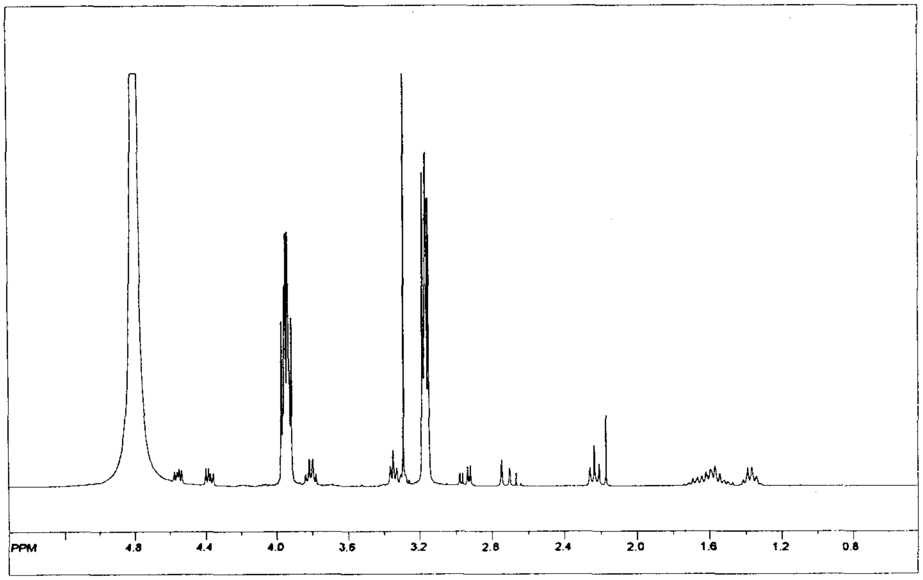

Figure 4.4: ^1H NMR of the ligand mixture (in D_2O) of **2**·($2H^+$):**7**·($2H^+$) *at a 1:0.1 molar ratio.*

FAB analysis of **2**·($2H^+$):**7**·($2H^+$) showed the two expected peaks of 140.0 and 366.1 $(M-H)^-$, respectively. Estimation of the ligand ratio on the surface of the NPs formed by method **A,** was done using citrate buffer solution (vide supra) and was calculated to be approximately 10% for **7**·(2H$^+$). Synthesis of **8**·(2H$^+$) followed exactly the same procedure as for **7**·(2H$^+$), and the NMR data obtained was in accordance to what was expected, with FAB analysis confirming the ligand with a mass of 613.2 (M-H)$^-$.

4.2.2.2 Particle size analysis

Particle size analysis of **2**:**7**·LaF$_3$:Ce,Tb by AFM analysis showed that they are within experimental error of **2**·LaF$_3$:Eu, and displayed a similar size distribution (10 nm diameter with a size distribution from 5-40 nm). This is in accordance to what was expected due to the fact that at a 10% molar ratio of **7**·(2H$^+$), the surface coverage of the longer ligand is insufficient to shift the size distribution beyond the measuring error (± 2.5 nm). AFM measurements of **2**:**8**·LaF$_3$:Ce,Tb was unsuccessful due to difficulties with particle suspension and agglomeration, however DLS experiments, under the same conditions as for **2**:**7**·LaF$_3$:Ce,Tb, gave an effective diameter of 14.6 nm, with a similar size distribution. Though no AFM analysis was successful as a comparison, an average particle size increase of 2-3 nm by DLS seems reasonable in solution when only 10% of the NP is coated with the longer ligand **8**·(2H$^+$).

4.2.2.3 Spectroscopic analysis

Analysis of the emission spectra in Figure 4.5 of **2**:**7**·LaF$_3$:Eu from method **A** & **B** show the same I_{7F2}/I_{7F1} intensity ratio of 1.6, with the enlarged area showing the deconvolution of the 578 nm peak. Due to the similarity in luminescent properties of **2**:**7**·LaF$_3$:Eu and **2**:**8**·LaF$_3$:Eu, only the former is shown for clarity. Luminescent lifetimes of the NPs were within experimental error of each other and of **2**·LaF$_3$:Eu (at three exponential lifetime fittings), at 6.5 ms (51%), 2.9 ms (41%) and 0.9 ms (8%). Synthesis of **2**:**7**·LaF$_3$:Er by method **A** shows the expected Er^{3+} transition ($^4I_{3/2}$-$^4I_{15/2}$) at 1530 nm, with a decay curve that was fitted with 3 exponentials, yielding lifetime values of 63 μs (39%), 14 μs (44%), and 3 μs (17%). Refer to Table 4.1 for full lifetime data.

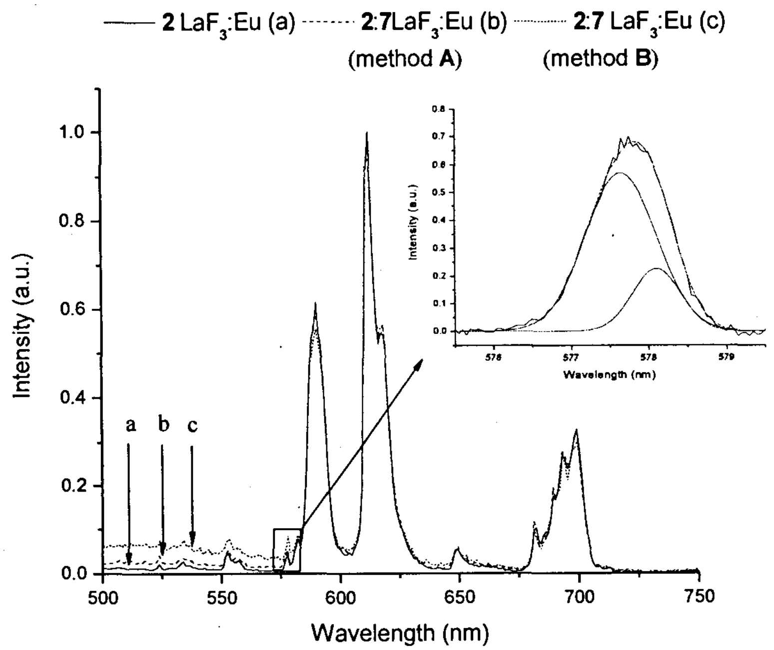

Figure 4.5: Emission spectra of surface reacted **2**·*LaF$_3$:Eu (line a),* **2**:**7**·*LaF$_3$:Eu by method* **A** *(line b), and* **2**·*LaF$_3$:Eu reacted with* **5** *by method* **B** *(line c). The spectra are offset for clarity. The inset shows the deconvolution of the high resolution (0.05 nm) 578 nm peak. (λ_{ex} = 397 nm).*

4.2.2.4 Quantum yield analysis

The quantum yields for **2**:**7**·LaF$_3$:Ce,Tb and **2**:**8**·LaF$_3$:Ce,Tb (by method **A**) were calculated to be 16% and 19%, respectively, and are within experimental error of each other (± 2%).[7] Furthermore, **2**:**8**·LaF$_3$:Ce,Tb at a 20% ligand molar ratio, was calculated to have a quantum yield of 9%, which is approximately half of its 10% ligand molar equivalent (Φ = 19%). In relation to a quantum yield of 20% for **2**·LaF_3:Ce,Tb, the above values (at 10% ligand molar ratio) are slightly lower and is likely a result of slight differences in NP formation. Shown in Figure 4.6a and 4.6b are the overlays of the emission spectra of **2**:**8**·LaF_3:Ce,Tb (method **A**) and quinine sulphate, at a 10% and 20% molar ratio respectively. As can be seen, the emission intensity of Ce^{3+} in Figure 4.6a is significantly lower than its counter part in Figure 4.6b, with respect to the Tb^{3+} intensity, indicating that less energy transfer is occurring from the Ce^{3+} ions to the Tb^{3+} ions. This effect is likely due to the bulkier nature of **8**·($2H^+$), in relation to **7**·($2H^+$), causing differences in NP formation dynamics, in which the distribution of Ce^{3+} ions to Tb^{3+} ions may not be as uniform within the NP matrix. at 20%) could not be made due to product insolubility.

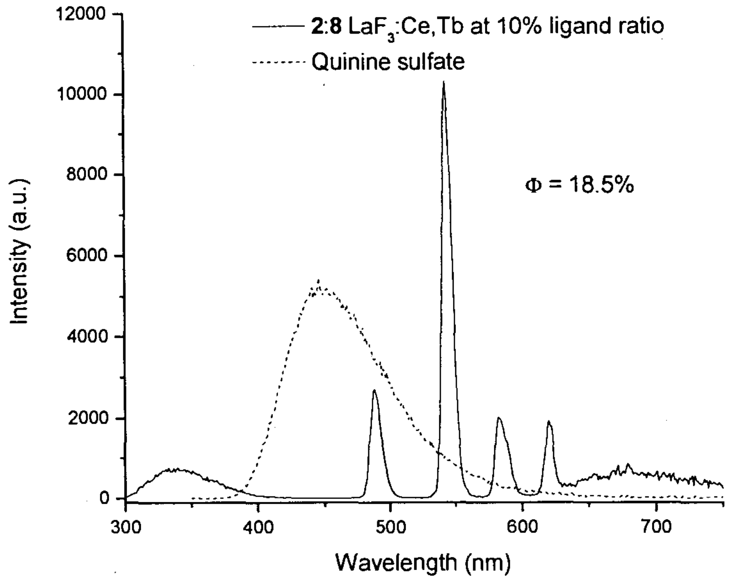

Figure 4.6a: Overlaid emission spectra of 2:8·LaF_3:Ce,Tb at 10% ligand molar ratio and quinine sulphate. The broad peak seen from 650 - 750 nm is due to second-order reflection of the 350 nm band. (λ_{ex} = 282 nm).

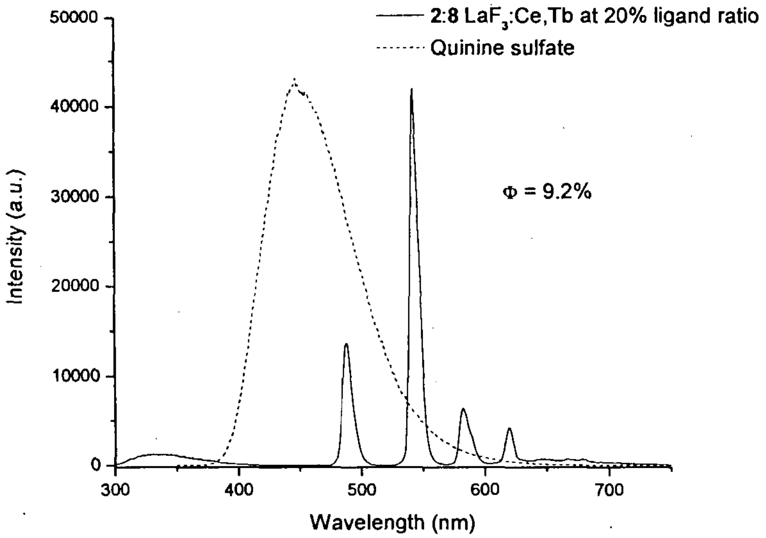

Figure 4.6b: Overlaid emission spectra of 2:8·LaF$_3$:Ce,Tb at 20% ligand molar ratio and quinine sulphate. The broad peak seen from 650 - 750 nm is due to second-order reflection of the 350 nm band. (λ_{ex} = 282 nm).

As for NPs made by method **B**, the measured quantum yield of **2**:**7**·LaF$_3$:Ce,Tb was 13%. Though the nature of method **B** is such that it uses **2**·LaF$_3$:Ce,Tb (Φ = 20%) as a platform to carry out the surface modification, it is suspected that the decrease in quantum yield over the unmodified NPs is due to the ligands coming off the surface of the NP while reacting with **6**. Consequently, if the ligands do not "re-coordinate" to the surface, which has been seen from the ^{1}H NMR of the supernatant collected from purification steps, the formation of surface quenching sites (ie: bare patches) may have contributed to the measured decrease in quantum yield, by either quenching energy transfer from Ce^{3+} to Tb^{3+}, or Tb^{3+} luminescence itself. Compound **2**:**8**·LaF$_3$:Ce,Tb by method **B** was not made. Refer to Table 4.2 for full quantum yield data.

4.3 Biotin-Avidin binding

To test the ability for the biotin-functionalized NPs to be bound to a biological system, avidin-coated agarose (AA) beads were used as a SPS for NP immobilization for the binding experiments. In principle, due to the fact that **2**:**7**/**2**:**8**·LaF_3:Ln^{3+} have ligand terminated biotin moieties on their outer surface, biotin binding to the AA beads with a large excess of NPs should be nearly quantitative and irreversible, allowing the excess of unbound NPs to be washed away. Experimentally, biotin-avidin binding was carried out by a suspension of AA beads in a borate buffer solution (BBS, pH = 9.1), followed by the addition of an excess of NPs dissolved in BBS and allowing the system to incubate at 21 °C for 0.5 hr. The coated AA beads were then washed three times with BBS to remove any unbound NPs. The need for the buffer solution is due to the zwitterionic nature of the proteins, which must be maintained in order to prevent denaturing of the protein.[8]

Control experiments with **2**·LaF_3:Eu shows that they physically adsorbed onto the surface of the AA beads; masking the emission of the biotin-based NP that are subsequently added. As such, the AA beads were exposed to a solution of **2**·LaF_3:Gd at 80% (use of a non-luminescent NP prevents signal overlap of the physically adsorbed NPs to the biotin-avidin bound NPs), followed by the addition of **2**:**7**·LaF_3:Eu^{3+}. Fluorescent studies of above-coated AA beads showed no europium signal, suggesting that the level of non-specific adsorption (of at least the non-luminescent NPs) is too high due to the charged surface of the NPs.

The overall negative charge of ligands that are bound to the surface are compensated for by excess La^{3+} ions. However at pH > 9 (due to BBS), the reduction in charge compensation from the un-protonated amino group yields an increase in the negative charge of the particle (as shown in Figure 4.7), which consequently results in high levels of electrostatic (non-specific) binding of the NP to the positively charged AA beads.

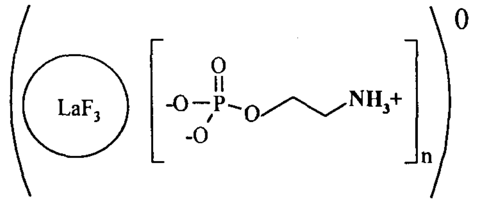

At pH < 9, the ligand has a protonated amino group.

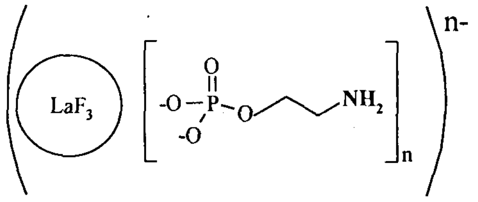

At pH > 9 (in BBS) the ligand has an un-protonated amino group.

Figure 4.7: Schematic diagram of the possible change in net charge that can occur to the NP upon addition of BBS.

4.4 Conclusions

Nanoparticle modification by means of functionalizing the surface with biotin-based ligands, by either NP synthesis (method **A**) or surface reaction (method **B**), afforded NPs with little change in their physical or luminescent properties, in relation to the reference 2-aminoethyl phosphate-based NPs (Chapter 3). Analysis of luminescent decay lifetimes were within experimental error of the reference NPs.

Quantum yield calculations were found to be within experimental error of the reference materials, with an average value of 18% by method **A** at a 10% molar ratio of the biotin-based ligand. NPs made with a 20% molar ratio of the biotin ligand, and those that were made by method **B**, showed lower quantum yield values, which is likely attributed to either an increase in surface quenching sites or a less random distribution of the Ce^{3+} ions, resulting in reduced energy transfer. Near infrared (NIR) analysis of the NPs doped with Er^{3+} ions, in D_2O, showed the expected transition at 1530 nm, with luminescent lifetime values within experimental error of the reference NIR reference materials.

Initial control experiments for the biotin-avidin binding experiments showed high levels of non-specific binding; using non-luminescent NPs to quench non-biotin binding sites, the subsequent addition of luminescent NPs for biotin-specific binding yielded no luminescence.

4.5 Tables

Compound	**Solvent**	**Ligand molar ratio to 2**	τ_1	τ_2	τ_3
2:**4**·LaF_3:Eu	H_2O	1:0.2	6.1 ms (54%)	2.3 ms (38%)	0.8 ms (8%)
Surface reaction of **2**·LaF_3:Eu with **3**	H_2O	unknown	6.1 ms (53%)	2.5 ms (38%)	0.9 ms (9%)
2:**4**·LaF_3:Er	D_2O	1:0.2	50 μs (32%)	12 μs (43%)	3 μs (25%)
2:**7**·LaF_3:Eu (method **A**)	H_2O	1:0.1	6.5 ms (51%)	2.9 ms (41%)	0.9 ms (8%)
2:**7**·LaF_3:Eu (method **B**)	H_2O	unknown	6.1 ms (55%)	2.5 ms (38%)	0.9 ms (7%)
2:**7**·LaF_3:Er (method **A**)	D_2O	1:0.1	63 μs (39%)	14 μs (44%)	3 μs (17%)
2:**8**·LaF_3:Eu (method **A**)	H_2O	1:0.1	6.5 ms (54%)	2.7 ms (36%)	0.9 ms (7%)

Error on the measured τ values is ± 5% for duplicates.

Table 4.1: Luminescent lifetimes (and percent contribution)

Compound	**Solvent**	**Ligand molar ratio to 2**	**Φ (%)**
2·LaF_3:Ce,Tb	H_2O	100%	20
2:**7**·LaF_3:Ce,Tb (method **A**)	H_2O	1:0.1	16
2:**7**·LaF_3:Ce,Tb (method **B**)	H_2O	unknown	13
2:**8**·LaF_3:Ce,Tb (method **A**)	H_2O	1:0.1	19
2:**8**·LaF_3:Ce,Tb (method **A**)	H_2O	1:0.2	9

Error on the measured Φ values is ± 2% for duplicates.

Table 4.2: Quantum Yields

4.6 Experimental

4.6.1 Experimental conditions

All chemicals were obtained from Aldrich and used without further purification unless otherwise indicated. Heterobifunctional cross-linker **6** was obtained from Quanta BioDesign and used without further purification. Source of water used consisted of distilled water. Nanoparticles (NPs) with the matrix composition LaF_3:Eu/Er were made with LaF_3 at 5% Eu^{+3} or Er^{3+} atom doping on the total Ln^{3+} amount. Nanoparticles (NPs) with the matrix composition LaF_3:Ce,Tb matrix, with La^{3+} at 40%, Ce^{3+} at 45%, and Tb^{3+} at 15% atom doping on the total Ln^{3+} amount.[7] Nanoparticles with the matrix composition GdF_3:La were made at 20% La^{3+} atom doping on the total Ln^{3+} amount. The reference material for quantum yield calculations was quinine sulfate in a 1M H_2SO_4 solution, with $\Phi_{ref} = 55\%$. The equation used to calculate the quantum yield is defined below where n is refractive index, I is the measured intensity, and A is the absorbance of the solution, and

Φ_{ref} is the quantum yield of the reference material. The error was estimated at 2% for duplicate measurements.

$$\Phi = \left[\frac{n^2_{sample} I_{sample} A_{ref}}{n^2_{ref} I_{ref} A_{sample}}\right] \Phi_{ref}$$

No NMR analysis was carried out on Er^{3+}, Tb^{3+} and Gd^{3+}-based NPs due to severe line broadening. All other experimental conditions used are the same as those stated in section 3.5 (Chapter 3).

4.6.2 Synthesis

2-(acrylamido)ethyl dihydrogen phosphate (**4**·(2H$^+$)): In 4 ml of water at 37 °C, **2**·(2H$^+$) (0.14 g, 1.0 mmol) was added, neutralized with $NaOH_{(aq)}$ to a pH of ~ 7, followed by the addition of **3** (0.27 g, 1.6 mmol) dissolved in 4 drops of DMSO. The reaction was stirred for 1 hr at 37 °C. Separation was carried out by extracting the impurities with 20 ml of diethyl ether, isolating the aqueous phase, removing the water by rotary evaporation at 80 °C, and drying overnight under reduced pressure. The isolated product was a white solid. Some *N*-hydroxysuccinimide and hydrolyzed phosphates were present. ^{1}H NMR: δ (D_2O) 6.4-6.1 (m, 2H, -CH_a=$CH_{,b,c}$), 5.7 (dd, $^3J_{cis}$ = 10.3 Hz, $^2J_{gem}$ = 1.5 Hz, 1H, -CH=$CH_{c,b}$), 3.8 (dt, $^3J_{HP}$ = 6.6 Hz $^3J_{gem}$ = 5.9 Hz, 2H, OCH_2CH_2NH-), 3.4 (t, $^3J_{gem}$ = 5.9 Hz, 2H, -OCH_2CH_2NH-); ^{13}C NMR: δ (D_2O) 177.6 (s, H_2C=CH-CO-N), δ 130.4 (s, H_2C=CH-), 127.8 (s, H_2C=CH-), 63.2 (d, $^2J_{P\text{-}C}$ = 5.5 Hz, $POCH_2CH_2NRH$), 40.3 (d, $^3J_{P\text{-}C}$ = 6.8 Hz, $POCH_2CH_2NRH$), 25.6 (s, -$CO(CH_2)_2CO$-); ^{31}P NMR: δ (D_2O) 0.6 (s, O_3PO-R).

2$\cdot$($2H^+$):4$\cdot$($2H^+$) at 1:0.2 molar ratio: In 4 ml of water at 37 °C, **2**$\cdot(2H^+)$ (0.14 g, 1.0 mmol) was added, neutralized with $NaOH_{(aq)}$ to a pH of ~ 7, followed by the addition of **3** (0.03 g, 0.2 mmol) in 4 drops of DMSO. The reaction was stirred for 1 hr at 37 °C. Separation was carried out by extracting with 20 ml of diethyl ether, isolating the aqueous phase, removing the water by rotary evaporation at 80 °C, followed by drying overnight under reduced pressure. The isolated mixture was a white solid. Refer to Chapter 3 for NMR assignments of **4**$\cdot(2H^+)$ and **2**$\cdot LaF_3$:Eu.

2:4$\cdot$$LaF_3$:Eu: NP synthesis followed the same procedure used for **2**$\cdot LaF_3$:Eu, but with a mixture of **2**$\cdot(2H^+)$ and **4**$\cdot(2H^+)$ at 1:0.2 molar ratio. ^1H NMR: δ (D_2O) 6.2 (bs, $\mathbf{CH_a}$=$\mathbf{CH_{b,c}}$), 5.8 (bs, CH_a=$\mathbf{CH_{c,b}}$-), 4.0 (bs, O$\mathbf{CH_2}$$CH_2$N-), 3.2 (bs, $OCH_2$$\mathbf{CH_2}$N-); ^{31}P NMR: δ (D_2O) 1.3 (bs, O_3**P**O-R) and -1.5 (very bs, O_3**P**O-R).

2$\cdot$$LaF_3$:Eu by surface reaction with 3: In 4 ml of H_2O, **2**$\cdot LaF_3$:Eu (0.1 g) was dissolved in water and heated to 37 °C under constant stirring, followed by the addition of **3** (7.1 mg, 0.04 mmol) dissolved in 4 drops of DMSO. Separation was carried out by extracting the impurities with 20 ml of ether, isolating the aqueous phase, and removing the water by rotary evaporation until a paste-like consistency remained. The product was purified by dissolving in 2 ml of water followed by the addition of acetone to form a precipitate, isolated by centrifuge, and dried under reduced pressure. ^1H NMR: δ (D_2O) 6.2 (bs, $\mathbf{CH_a}$=$\mathbf{CH_{b,c}}$), 5.8 (bs, CH=$\mathbf{CH_{c,b}}$), 4.0 (bs, O$\mathbf{CH_2}$$CH_2$N-), 3.2 (bs, $CH_2$$\mathbf{CH_2}$N-).

2:4$\cdot$$LaF_3$:Er: Same procedure as above, but with $Er(NO_3)_3\cdot 5H_2O$ (0.03 g, 0.27 mmol).

2$\cdot$($2H^+$):7$\cdot$($2H^+$) at 1:0.1 ligand molar ratio: ligand **2**$\cdot(2H^+)$ (0.14g, 1.02 mmol) was dissolved in 4 ml of water, neutralized with NaOH $_{(aq)}$, followed by the addition of **5** (0.03 g, 0.09 mmol) dissolved in a minimum of DMSO. The solution was stirred for 1 hr at 37

°C, and isolated by precipitating with acetone and centrifuging the precipitate. Refer to Figure 4.8 for atom labelling. ^{1}H NMR: δ (D$_2$O) 4.6 (dd, $^3J_{cis}$ = 7.6 Hz, $^2J_{gem}$ = 5.4 Hz, 1H, Hb), 4.4 (dd, $^3J_{cis}$ = 8.0, $^2J_{gem}$ = 4.5, 1H, Hc), 3.9 (dt, $^3J_{HP}$ = 7.4 Hz, $^3J_{vic}$ = 6.7 Hz, 19H, POC**H**$_2$CH$_2$NH$_2$), 3.8 (dt, $^3J_{HP}$ = 7.4 Hz, $^3J_{vic}$ = 6.7 Hz, 2H, POC**H**$_2$CH$_2$NHR), 3.4 (t, $^3J_{vic}$ = 5.0 Hz, 2H, POCH$_2$C**H**$_2$NHR), 3.4-3.3 (m, 1H, Ha), 3.2 (t, $^3J_{vic}$ = 5.0 Hz, 19H, POCH$_2$C**H**$_2$NH$_2$), 3.0 (dd, $^3J_{cis}$ = 13.0 Hz, $^2J_{gem}$ = 4.5 Hz, 1H, Hd), 2.7 (dd, 3J_{cis} = 13.0 Hz, 1H, He), 2.2 (t, dd, $^3J_{cis}$ = 7.5 Hz, 2H, H_{c1}), 1.7 (m, 2H, H_{c2}), 1.5 (m, 2H, H_{c3}), 1.4 (m, 2H, H_{c4}); ^{13}C NMR: δ (D$_2$O) 177.2 (-**C**=O), 63.0 (POC-**C**-NHR), 62.0 (C$_6$), 60.5 (PO-C-**C**-NH$_2$), 60.3 (C$_7$), 55.3 (C$_5$), 40.5 (PO-**C**-C-NH$_2$), 40.3 (PO-**C**-C-NHR), 39.7 (C$_8$), 35.5 (C$_1$), 27.8 (C$_4$), 27.6 (C$_2$), 25.2 (C$_3$); ^{31}P NMR: δ (D$_2$O) 3.7 (s, O$_3$**P**O-R), 2.8 (s, O$_3$**P**O-R-biotin).

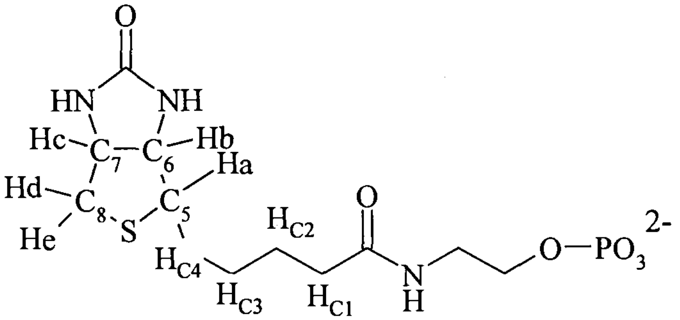

Figure 4.8: Atom labelling of ligand 7·(2H$^+$).

2:7·LaF$_3$:Eu (method A): NP synthesis followed the same procedure used for **2**·LaF$_3$:Eu, but with a mixture of **2**·(2H$^+$) and **7**·(2H$^+$) at 1:0.1 molar ratio. ^{1}H NMR: δ (D$_2$O) 4.7 (bs, Hb), 4.5 (bs, Hc) 4.1 - 3.5 (bs, OC**H**$_2$CH$_2$N-), 3.4 - 2.2 (bs: OCH$_2$C**H**$_2$N-, Ha, Hd, and H_{c1}), 2.0 - 1.0 (bs: H_{c2}-H_{c4}).

2:7·LaF$_3$:Eu by surface reaction (method B): In 4 ml of H$_2$O, **2**·LaF$_3$:Eu (0.1 g) was dissolved in 4 ml of water and heated to 37 °C under constant stirring, followed by the addition of **5** (3.4 mg) dissolved in 4 drops of DMSO. The solution was allowed to stir for

1 hour. The product was isolated by precipitating with acetone, centrifuging the precipitate, and drying under reduced pressure. ^{1}H NMR: δ (D_2O) 4.7 (bs, Hb), 4.5 (bs, Hc) 4.1 - 3.5 (bs, OCH_2CH_2N-), 3.4 - 2.2 (bs: OCH_2CH_2N-, Ha, Hd, and H_{c1}), 2.0 - 1.0 (bs: H_{c2}-H_{c4}).

2:7·LaF$_3$:Er: Same procedure as **2**:7·LaF_3:Eu (method **A**), but with $Er(NO_3)_3 \cdot 5H_2O$ (0.03 g, 0.27 mmol).

2:7·LaF$_3$:Ce,Tb: Same procedure as **2**:7·LaF_3:Eu (method **A**), but with $Ce(NO_3)_3 \cdot 5H_2O$ (0.58 g, 1.31 mmol), $Tb(NO_3)_3 \cdot 6H_2O$ (0.21 g, 0.55 mmol) and $La(NO_3)_3 \cdot 6H_2O$ (0.55g, 1.26 mmol).

2·(2H$^+$):8·(2H$^+$) at 1:0.1 ligand molar ratio: Ligand **2**·(2H$^+$) (0.14 g, 1.02 mmol) was dissolved in 4 ml of water, neutralized with NaOH $_{(aq)}$, followed by the addition of **6** (0.05 g, 0.08 mmol) dissolved in a minimum of DMSO. The solution was stirred for 1 hr at 37 °C, and isolated by precipitating with acetone and centrifuging the precipitate. Refer to Figure 4.9 for atom labelling. ^{1}H NMR: δ (D_2O) 4.6 (dd, $^3J_{cis}$ = 7.6 Hz, $^2J_{gem}$ = 5.4 Hz, 1H, Hb), 4.4 (dd, $^3J_{cis}$ = 8.0 Hz, $^2J_{gem}$ = 4.5 Hz, 1H, Hc), 4.0 (dt, $^3J_{HP}$ = 7.4 Hz, $^3J_{vic}$ = 6.7 Hz, 10H*, $POCH_2CH_2NH_2$), 3.9 (dt, $^3J_{HP}$ = 7.4 Hz, $^3J_{vic}$ = 6.7 Hz, 1H*, $POCH_2CH_2NHR$), 3.8 (t, $^3J_{vic}$ = 5.9 Hz, 2H, H_{c10}), 3.7 (range) (m, 12H, $(C_2H_4O)_3$), 3.5 (t, $^3J_{vic}$ = 5.3 Hz, 2H, H_{c11}), 3.45 (t, $^3J_{vic}$ = 5.0 Hz, 1H*, $POCH_2CH_2NHR$), 3.38 (t, $^3J_{vic}$ = 5.0 Hz, 2H, H_{c9}), 3.38-3.32 (m, 1H, Ha), 3.2 (t, $^3J_{vic}$ = 5.0 Hz, 10H*, $POCH_2CH_2NH_2$), 3.0 (dd, $^3J_{cis}$ = 13.0 Hz, $^2J_{gem}$ = 4.5 Hz, 1H, Hd), 2.8 (dd, $3J_{cis}$ = 13.0 Hz, 1H, He), 2.6 (t, $^3J_{vic}$ = 6.0 Hz, 2H, H_{c12}), 2.3 (t, $^3J_{cis}$ = 6.6 Hz, 2H, H_{c1}), 1.7 (m, 2H, H_{c2}), 1.5 (m, 2H, H_{c3}), 1.4 (m, 2H, H_{c4}). * The number of protons of **2** are in relation to **8** for clarity.

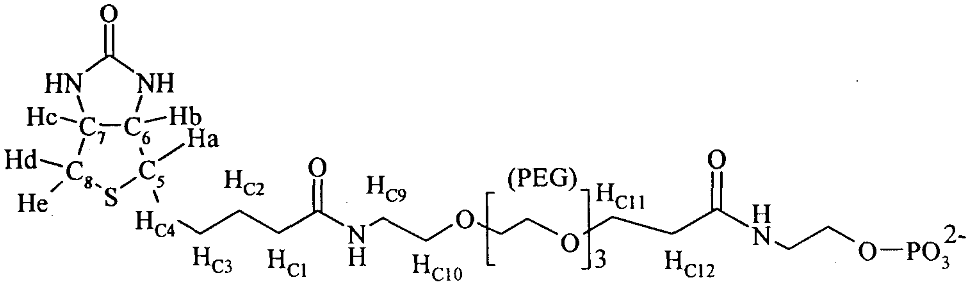

Figure 4.9: Atom labelling of ligand 8·(2H⁺).

2:8·LaF₃:Eu (method A): Same procedure as **2**:**8**·LaF₃:Eu (method **A**), but with the respective ligand **8**·(2H⁺). ¹H NMR: δ (D_2O) 4.7 (bs, Hb), 4.5 (bs, Hc) 4.1 - 3.7 (bs, OCH_2CH_2N-) 3.6 - 3.4 (bs: H_{c10},$(PEG)_3$,H_{c11}), 3.3 - 2.2 (bs: OCH_2CH_2N-, Ha, Hd, H_{c12} and H_{c1}), 2.0 - 1.0 (bs: H_{c2}-H_{c4}).

2:8·LaF₃:Er: Same procedure as **2**:**8**·LaF₃:Eu (method **A**), but with $Er(NO_3)_3 \cdot 5H_2O$ (0.03 g, 0.27 mmol).

2·(2H⁺):8·(2H⁺) at 1:0.2 ligand molar ratio: Same procedure as for **2**·(2H⁺):**8**·(2H⁺) at 1:0.1 ligand molar ratio, but with **2**·(2H⁺) (0.06 g, 0.43 mmol) and **6** (0.05 g, 0.08 mmol). See **2**·(2H⁺):**8**·(2H⁺) at 1:0.1 ligand molar ratio for NMR characterization.

2:8·LaF₃:Ce,Tb at 10% ligand molar ratio (method A): Same procedure as **2**:**7**·LaF₃:Eu (method **A**), but with $Ce(NO_3)_3 \cdot 5H_2O$ (0.58 g, 1.31 mmol), $Tb(NO_3)_3 \cdot 6H_2O$ (0.21 g, 0.55 mmol) and $La(NO_3)_3 \cdot 6H_2O$ (0.55g, 1.26 mmol).

2:8·LaF₃:Ce,Tb at 20% ligand molar ratio (method A): Same procedure as **2**:**8**·LaF₃:Ce,Tb at 10% ligand molar ratio (method **A**), but with **2**·2H⁺ with **6** at a 1:0.2 ligand molar ratio, respectively.

2·GdF₃:La at 20%: Same procedure as **2**·LaF₃:Eu, but at 75°C with $La(NO_3)_3 \cdot 6H_2O$ (0.12 g, 0.27 mmol) and $Gd(NO_3)_3 \cdot 6H_2O$ (0.59 g, 1.32 mmol).

NP-avidin binding: Avidin-agarose beads (supplied from Aldrich) (70 μl) were suspended in 0.3 ml of borate buffer solution (BBS), followed by the addition of **2**·GdF_3:La (5 mg) in 0.5 ml of water. The solution was allowed to incubated for 0.5 hr at 21 °C. The avidin-agarose beads were washed three times with water, then re-suspended in 0.3 ml of BBS, followed by the addition of **2**:**7**·LaF_3:Eu (5 mg) in 0.5 ml of water. The solution was allowed to incubate for 3 hrs at 21 °C.

4.7 References

[1] C. Sun, J. Yang, L. Li, X. Wu, Y. Liu, S. Liu (2004) *J. Chromatogr. B* **803**, 173-190.

[2] K. Aslan, C.C. Luhrs, V.H. Perez-Luna (2004) *J. Phys. Chem. B*, **108**, 15631-15639.

[3] N. Weibel, L.J. Charbonnière, M. Guardigli, A. Roda, R. Ziessel (2004) *J. Am. Chem. Soc.* **126**, 4888- 4896.

[4] M.J Roberts, M.D. Bentley, J.M. Harris (2002) *Adv. Drug Deliv. Rev.* **54**, 459-476.

[5] M. Wilchek, E.A. Bayer (1999) *Biomol. Eng.* **16**, 1-4.

[6] http://www.seradyn.com/technical/pdf/PowerbindTN.pdf.

[7] J. W. Stouwdam, G.A. Hebbink, J. Huskens, F.C.J.M. van Veggel (2003) *Chem. Mater.* **15**, 4604-4616.

[8] http://www.amresco-inc.com/catalog/PDF/Buffers.pdf.

Chapter 5

Summary

Chapter 1 covers the basic properties of lanthanide ions, and their use in various matrices. Most of the emphasis is on the historical developments of water-soluble lanthanide complexes, in which the three most common ligand derivatives, β-diketonate, phenanthroline, and salicylic acid, were discussed in some detail. Though in many cases the complexes are stable in aqueous environments, many of the complexes suffer from short luminescent lifetimes and low quantum yields, due to poor shielding from solvent quenching effects. This is particularly relevant for the near-infrared (NIR) emitting complexes which are very sensitive to solvent (OH-related) and other luminescent quenching sources. Improvements to the lanthanide ion luminescence are discussed by means of three different nanoparticle (NP) methodologies: (1) carboxyl-modified polystyrene NPs which are impregnated with Eu^{3+}- and Tb^{3+}-based chelates, (2) fluorescent oxide NPs via YVO_4^{3-} and (3) LaF_3 matrices. Of the three methodologies, the latter system offers a host matrix with the lowest phonon energy (350 cm^{-1}), thereby increasing luminescent lifetime due to the minimal vibrational quenching from the host material.

NP-based materials has become fairly wide-spread, with particular interest in the area of biological applications, for which the use of various NP systems, including gold NPs and quantum dots (QDs), is covered in Chapter 2. Emphasis is placed on the various strategies of linking NPs to biological macromolecules. The concept and application of several heterobifunctional cross-linkers (HBCs) is explained, whereby the termini of the linkers can easily be modified with reactive-specific derivatives, such as, but not limited to, *N*-hydroxysuccinimide (NHS) for amine specific reactions, maleimide for thiol specific reactions, and biotin for avidin/streptavidin binding systems. Ultimately, these systems allow for controlled attachment of NPs in aqueous conditions, without significantly affecting their luminescent properties.

The development of hydrophilic NPs with phosphate-based poly(ethylene glycol) (PEG), and amine-terminated ligands is described in Chapter 3. Use of PEG is commonplace in many biological applications, due to its water-solubility and established biocompatibility. Use of the amine-terminated ligand allowed for the development of a one-step method to produce NPs that can be attached directly to HBCs through a primary amine, without the need for any preliminary surface modifications. Of the two ligands used, the latter yielded NPs that when doped with Eu^{3+} and Er^{3+}, yielded luminescent lifetimes that were at least twice as long as the PEG-based NPs with a measured quantum yield of 20% in water.

From that point, development of alternate routes to attach HBCs to the surface of the amine-terminated NPs yielded two methods in Chapter 4. The first method provides a way for a predefined ratio of ligand-to-HBC to be made prior to NP formation, thereby controlling the concentration of HBC to be loaded on the surface of the NP. The second method involves the direct reaction the HBC with the NP surface, forgoing control over the level of HBC loaded on the NP. In both cases, the emission spectra, luminescent lifetimes and quantum yields measured were within error of each other. Furthermore, the NPs were modified with biotin-based HBCs in order to test its binding ability to avidin-coated agarose beads. It was found that high levels of non-specific binding of non-biotin labeled NPs prevented the binding of the biotin-based NPs. This effect was attributed to electrostatic attraction of the positively charged avidin beads to the negatively charged NPs.